Review

CrossMark
click for updates

Authors for correspondence:
Lise-Marie Lacroix
e-mail: lmlacroi@insa-toulouse.fr
Fabien Delpech
e-mail: fabien.delpech@insa-toulouse.fr

New generation of magnetic and luminescent nanoparticles for *in vivo* real-time imaging

Lise-Marie Lacroix[1,2], Fabien Delpech[1,2], Céline Nayral[1,2], Sébastien Lachaize[1,2] and Bruno Chaudret[1,2]

[1]INSA, UPS, LPCNO (Laboratoire de Physique et Chimie des Nano-Objets), Université de Toulouse, Toulouse 31077 France
[2]UMR 5215, LPCNO, CNRS, Toulouse 31077, France

A new generation of optimized contrast agents is emerging, based on metallic nanoparticles (NPs) and semiconductor nanocrystals for, respectively, magnetic resonance imaging (MRI) and near-infrared (NIR) fluorescent imaging techniques. Compared with established contrast agents, such as iron oxide NPs or organic dyes, these NPs benefit from several advantages: their magnetic and optical properties can be tuned through size, shape and composition engineering, their efficiency can exceed by several orders of magnitude that of contrast agents clinically used, their surface can be modified to incorporate specific targeting agents and antifolding polymers to increase blood circulation time and tumour recognition, and they can possibly be integrated in complex architecture to yield multi-modal imaging agents. In this review, we will report the materials of choice based on the understanding of the basic physics of NIR and MRI techniques and their corresponding syntheses as NPs. Surface engineering, water transfer and specific targeting will be highlighted prior to their first use for *in vivo* real-time imaging. Highly efficient NPs that are safer and target specific are likely to enter clinical application in a near future.

1. Introduction

Since the discovery, by chance, of X-ray potentiality by Roentgen in 1896, imaging techniques have been optimized and extended. Depending on the penetration depth, the spatial resolution and the sensitivity required, X-ray-computed tomography (CT), positron emission tomography, magnetic resonance imaging (MRI) or optical imaging, such as near-infrared (NIR) fluorescent imaging, may be selected as the most relevant imaging modality [1]. In all cases, enhancement of the signal-to-noise ratio, and thus of the sensitivity of these imaging techniques, requires the introduction of contrast agents, such as radioisotopes, paramagnetic molecules or more recently inorganic nanoparticles (NPs) [2]. The latter have benefited from tremendous advances during the last two decades notably in terms of available synthetic routes. In particular, the improvements in solution-phase approaches now allow easy and low-cost access (compared with classical physical or vacuum methods) to well-controlled nano-probes. Prominent examples of imaging modalities which have profited from this intense research activity are MRI and NIR luminescence: a new generation of sophisticated nano-objects has reached such a stage of maturity, especially in terms of probe sensitivity, that their use has, on one hand, become standard practice in *in vitro* biology research and, on the other hand, holds promise for *in vivo* real-time detection.

This review intends to highlight these advances and developments that have occurred in the last few years for MRI and NIR luminescence detection. In the case of MRI, the upgrading of contrast agents based on oxide NPs to metallic NPs yields to strongly enhanced probe sensitivity. As will be detailed herein, this was achieved thanks (i) to the unprecedented magnetization related to the metallic
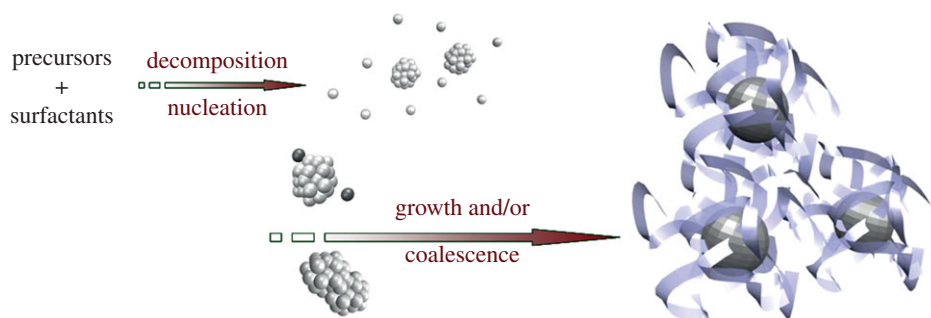
Figure 1. Schematic of the general mechanism driving chemical NP synthesis. (Online version in colour.)

nature of the NPs and (ii) to the narrow-size distribution allowing homogeneous and intense magnetic properties from one NP to another. Similarly, in the case of NIR, impressive progress has been realized on the synthesis of quantum dots (QDs) able to absorb and emit efficiently in the NIR range of wavelength (where the transmissivity of organic tissue is maximum). Additionally, following the trend towards 'greener' chemistry, new versions of QDs free of Cd, Pb and Hg are now available. These significant advances have motivated this review dedicated to an up-to-date perspective on magnetic NPs and NIR-emitting QDs. Moreover, because of different features in terms of sensitivity, resolution, acquisition time and operational costs, fluorescence-based *in vivo* imaging techniques are complementary to MRI [1]. NIR enables faster measurements with higher sensitivity [1,3,4], while MRI ensures a higher spatial resolution and depth of penetration. Thus, very recent work focused on bimodal NPs, i.e. combining MRI and NIR modalities, will also be addressed as challenging perspective in view of designing more and more sensitive probes and/or multifunctional theranostic nano-objects (MRI contrast agents can also be used as heating centres in magnetic hyperthermia) [5].

After a general introduction on liquid-phase synthesis of NPs, we will present the basics of MRI and the general chemical synthesis for a new generation of optimized contrast agents. NIR fluorescence technique requirements will then be discussed, optimal material being highlighted. Corresponding type I and type II QD synthesis will be listed. MRI and NIR contrast agents being prepared mostly in organic solvants, we will review the surface engineering strategies to ensure the water transfer of generic inorganic NPs and their further biodistribution and specific targeting. Up-to-date results of real-time *in vivo* MRI and NIR imaging obtained with the new generation of NPs will be reviewed before concluding with the requirements and the first promising attempt for NIR/MRI multi-functional NPs.

2. Liquid-phase synthesis of inorganic nanoparticles

This brief part aims at introducing the general principles of NP synthesis in solution to give the reader the keys to a deep understanding of the numerous synthesis examples presented hereafter (§§3.2 and 4.2). This review focuses on the chemical approach to NP formation particularly because of its ability to provide NP samples (i) of high quality and (ii) in adequate amounts for further biological use.

Colloidal solutions of NPs of various natures (metallic, semiconducting and oxides) can be prepared by a chemical approach. The general strategy followed relies on the decomposition of a precursor, typically a salt or an organometallic

compound (figure 1). This decomposition yields free atoms that tend to aggregate and form small seeds during the nucleation step. Metallic NP synthesis may require the use of a reducing agent to convert oxidized atoms (M^{n+}) into metallic atoms (M^0). The seeds formed during the nucleation step then grow by successive addition of atoms, by coalescence or through a ripening based process [6,7]. To prevent NPs from aggregation and sintering, organic molecules (surfactants) or polymers are added to ensure steric hindrance or electrostatic repulsion between NPs.

Since physical properties depend on the size, size distribution and shape of NPs, nucleation and growth steps must be carefully tuned. Monodisperse NPs (with a narrow size distribution $\sigma < 10\%$) can be prepared via burst nucleation, fast and limited in time, followed by homogeneous growth [8]. The extent of nucleation and growth steps depends of experimental parameters, such as reaction time, temperature, nature of the precursors and surfactants; thus careful optimization of these parameters are usually required [9].

3. Magnetic resonance imaging principle and nanomaterials

In this section, we will first introduce the basics of MRI, highlighting the requirements for optimized contrast agents: (i) high magnetization materials, (ii) large magnetic core size, and (iii) core accessibility to water protons. Up-to-date syntheses of magnetic NPs will then be reviewed in the context of *in vivo* MRI, i.e. (i) metallic material preferred to oxides owing to their enhanced magnetization and (ii) narrow size distribution to ensure homogeneity of the magnetic properties.

3.1. Basics of magnetic resonance imaging

Clinical MRI is based on the relaxation of the nuclear spin of water protons in a strong magnetic field (1.5–3 T in hospitals, 9 T or greater in laboratories). Into such a static field B_0, spins tend to align parallel or antiparallel (figure 2a), and process at the Larmor frequency ω_0 which is proportional to the field strength

$$\omega_0 = B_0 \cdot \gamma, \tag{3.1}$$

where γ is the gyromagnetic ratio (for hydrogen, $\gamma = 42{,}6$ MHz T^{-1}).

Once magnetized by the static field, protons can be excited through a perpendicular pulsed field B_1 (rotating around the B_0 axis at the Larmor frequency, i.e. in the radiofrequency (RF) range), which leads to a magnetization M_{xy} that is
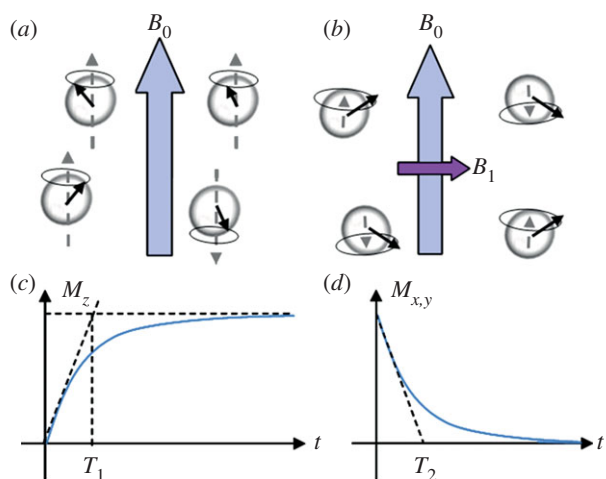
Figure 2. Schematic of water proton spins in (a) a static magnetic field B_0 and (b) upon RF-excitation dashed arrow represents M_z component, solid circle represents $M_{x,y}$ component. Evolution as a function of time of (c) M_z and (d) $M_{x,y}$ with, respectively, T_1 and T_2 as time constant derived from the initial slope (dashed lines). (Online version in colour.)

Figure 3. Schematic of a magnetic NP surrounded by water protons. Arrows indicate the magnetic field induced. (Online version in colour.)

perpendicular to B_0 (figure 2b). After the removal of the RF field, spins tend to realign with B_0 following (figure 2) a longitudinal relaxation (M_z increasing according to an exponential law, time constant T_1, figure 2d), and a transverse relaxation (exponential decay of M_{xy}, time constant T_2, figure 2e).

MR images are acquired while protons return to their equilibrium state, contrast being based on the difference in relaxation rate $R_i = 1/T_i$ ($i = 1$ or 2). Relaxation rate depends of numerous parameters, such as the surrounding medium, field strength, temperature, accessibility of protons and of course nature of the contrast agents. Intrinsically, tumour cells exhibit different relaxation constants compared with healthy surrounding tissues, which can lead to an MRI contrast. However, dedicated cancer imaging may require an enhancement of the signal-to-noise ratio.

The static magnetic field applied can be increased to accelerate the precession of spins (equation (3.1)) and to slightly improve the excess proportion of spins aligned parallel (low energy state). As the signal is linked with the relative magnetization of tissues, i.e. the spin excess, enhancement could be reached. However, establishing a large homogeneous field on the whole body is not technologically easy, thus improvement in signal at fixed magnetic field strength (up to 3 T), through the introduction of adequate contrast agents, is still required.

Paramagnetic, superparamagnetic or ferromagnetic contrast agents affect both relaxation processes [10]. However, depending of their nature, they will increase more specifically the relaxation rate R_1 (positive contrast agent) or R_2 (negative contrast agent). Paramagnetic ions (mainly gadolinium(III) complexes) have been widely used as positive contrast agents in clinical applications [11–13]. However, high doses of these toxic metal ions are required due to the relatively low efficiency of Gd-based contrast agents. For the last 20 years, NPs, including iron oxide NPs, have received lots of interest as efficient non-toxic R_2 contrast agents [14].

Magnetic NPs are small magnets that generate a magnetic field in their vicinity (figure 3). Such field inhomogeneity accelerates the phase decoherence of the spins [15]. Therefore, NPs act as negative contrast agents, their efficiency being quantified through the normalized relaxivity
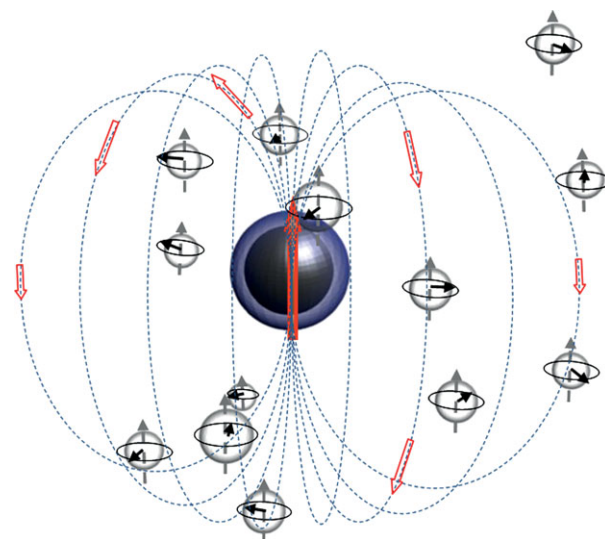
$r_2 = R_2/\text{concentration (mMol}^{-1}\,\text{s}^{-1})$. In a first approximation, relaxivity varies as the square of the magnetic field induced in the vicinity of the water proton. The magnetic field is a short-distance perturbation, which vanishes quickly

$$r \propto d^{-6}.(M_S V)^2, \qquad (3.2)$$

where d is the distance of the proton-centre of the magnetic NP, M_S the saturation magnetization and V the volume.

The accessibility of the water proton to the NP surface is of particular importance due to the d^{-6} decrease in r. Therefore, from a magnetic point of view, the coating of the magnetic core, which ensures the biostability of the inorganic NPs as described in §4, should be as thin as possible to yield high relaxivity (table 1). However, biostability often requires a relatively large coating, as discussed in §4; thus, a delicate balance should be found regarding the corona shell thickness.

In order to improve the relaxivity, larger NPs could also be used [24,25] (table 1), but size affects the magnetic behaviour of NPs. Small NPs (below 12 nm for Fe) behave as paramagnetic species (superparamagnetism): they can be easily magnetized under B_0 and do not exhibit magnetization in the absence of magnetic field (remnant state $M_r = 0$). Larger NPs are ferromagnetic and exhibit a net magnetization ($M_r \neq 0$). This difference of behaviour affects the stability of NPs in solution through the modification of dipolar interactions (in first approximation $\propto M_r^2$ [26]). Aggregation of the ferrofluid may arise for ferromagnetic NPs, thus, to date, superparamagnetic NPs have been prevailing material for *in vivo* applications. Recently, larger NPs with a peculiar magnetic configuration (vortex state) have been proposed for bioapplications [27]. These NPs exhibit very low magnetization in the absence of any applied field (weak M_r), resulting in weak interparticle interactions, but large volume and thus a presumably high relaxivity. Such vortex states are observed for the intermediate size range, typically 30–100 nm for iron [28,29].

In addition to size control, one can optimize M_S. Saturation magnetization is an intrinsic parameter of the material chosen and corresponds to the maximum magnetic moment that can be reached upon an applied field. Magnetic dopants, such as Mn, can be added to ferrite materials, leading to a slight increase in M_S (table 1). To further enhance M_S,

Table 1. r_2 relaxivities of magnetic NPs. CLIO: cross-linked iron oxide NPs, used in clinical applications. SPM, superparamagnetic; FM, ferromagnetic; DMSA, 2,3-dimercaptosuccinic acid; PEG, polyethylenglycol; TMAOH, tetramethylammonium hydroxide.

| material | M_S (emu/g_{metal}) | core size (nm) | magnetic state | organic corona | | r_2 (s^{-1} mM^{-1}) | B_0 (T) | refs |
				ligand	size (nm)			
CLIO-Fe$_x$O$_y$	—	—	—			62		[16]
Fe$_3$O$_4$	101	12	—	DMSA	2	218	1.5	[16]
	—	10	—	PEG PEI	7	40	1.5	[17]
	—	10	—	PEI	2	75	1.5	[17]
MnFe$_2$O$_4$	∼60	6	—	DMSA	2	208	1.5	[16]
	∼90	9	—	DMSA	2	265	1.5	[16]
	110	12	—	DMSA	2	358	1.5	[16]
Fe@Fe$_3$O$_4$	70	10	FM	PEG	2	129	1.5	[18]
	140	16	FM	DMSA	2	324	9.4	[19]
	112	15	FM	PEG	15	67	3	[20]
	164	15	FM	PEG	15	220	3	[20]
Co@Au	—	30–90	—			10^7	7	[21]
FeCo@C	162	4	SPM	PEG	17	185	1.5	[22]
	215	7	SPM	PEG	17	644	1.5	[22]
FePt	125	9	SPM	TMAOH	2	239	4.7	[23]

metals, such as Fe or Co, should be preferred to their oxide counterparts (table 1). Though contrast agents used clinically are nowadays only based on superparamagnetic iron oxide NPs [30], the design of optimized contrast agents would benefit from metallic NPs, providing that these NPs do not exhibit toxicity [31]. Thus, we will focus our discussion on the recent strategies developed to synthesize and protect metallic NPs with optimized properties.

3.2. Synthesis of magnetic nanoparticles

Multiple strategies have been developed to synthesize monodispersed iron oxide NPs (maghemite γ-Fe$_2$O$_3$ or magnetite Fe$_3$O$_4$), either in aqueous [32] or in organic solvents [33]. Size control could be reached by the decomposition of organometallic precursors at high temperature in the presence of long alkyl chain surfactants [34,35], further synthesis information being found in recent review articles [36,37]. Concerning magnetic dopants, they can be added in the spinel structure by co-reduction at high temperature of organometallic precursors, such as Mn(acac)$_2$ and Fe(acac)$_3$ [38].

Here, we will focus our attention on synthesis of metallic NPs, promising higher magnetization, as explained previously. Iron being highly reactive towards oxidation, metallic Fe NPs were mainly prepared in organic solvents (table 2) [56]. Classically, Fe(CO)$_5$ was decomposed at high temperature in the presence of long-chain amines [39,57]. Though highly toxic, this precursor benefited from Fe atoms already reduced (oxidation degree 0); therefore no reducing agents were required. However, the magnetic properties of the NPs obtained were generally lower than the bulk value, owing to their intrinsic carburation from CO byproduct [58]. To prevent such carburation, Fe(CO)$_5$ can be replaced by iron salts or organometallic compounds, whose decomposition did not yield any carbon source. Owing to their high stability,

the decomposition and reduction of iron salts required harsh conditions. For instance, FeCl$_2$ could be reduced in water by sodium borohydride, but boron contamination has been found to decrease the NP moment [18]. Therefore, decomposition of organometallic compounds such as Fe(C$_5$H$_5$)(C$_6$H$_7$) [19] or {Fe[N(SiMe$_3$)$_2$]$_2$}$_2$ [42,59] under dihydrogen atmosphere could be preferred to yield unoxidized iron NPs in mild conditions (bulk magnetization). Owing to its high reactivity, the latter amido precursor could also be reduced solely by a long-chain amine in the absence of H$_2$ [60]. The optimization of the nucleation and growth steps, through the tuning of experimental parameters (temperature and surfactants), yielded Fe NPs with unprecedented size and shape control in the range 1–100 nm (figure 4a,b).

Cobalt NPs can be prepared following similar procedures. Co$_2$(CO)$_8$ could be decomposed at high temperature to yield monodisperse NPs [44,62]. As observed for Fe, the binding of –CO species at the NPs' surface decreased their magnetic properties [63]. Cobalt salt (CoCl$_2$) can be reduced with a strong reducing agent (superhydride LiEt$_3$BH) and yield NPs of the ε-Co crystalline phase with degraded magnetic properties prior to annealing treatment [45]. Co can crystallize in a hexagonal close packed structure which exhibits optimized magnetic properties. Benefiting from the crystallographic unicity of the c-axis, intensive research has been devoted to the synthesis of anisotropic Co NPs. Polyol synthesis [46] along organometallic approaches [47,48] yielded single crystalline Co nanorods with a relatively narrow size distribution (figure 4c). Though nanorods have never been tested for MRI purposes, they could potentially present high relaxivity, analogous to elongated Co@Au nanowontons, prepared through physical process [21] (table 1).

To further enhance the magnetic moment, Fe or Co could be replaced by FeCo NPs, providing that highly crystalline NPs with optimized composition (60% Fe and 40% Co)

5

Table 2. Overview of the chemical approaches for the synthesis of metallic NPs. OA, oleic acid; OY, oleylamine; HDAHCl, hexadecylamonium chloride; NaOA, sodium oleate; PA, palmitic acid; HDA, hexadecylamine; LA, lauric acid; DDA, dodecylamine; PMMA, polymethylmethacrylate; PEG, polyethyleneglycol; TOP, trioctylphosphine; TOPO, trioctylphosphine oxide; DOA, dioctylamine; SA, Stearic acid.

| material	precursor	method	surfactants	temperature (°C)	core size (nm)	M_S (emu/g_{metal})	refs
Fe	Fe(CO)$_5$	thermodecomposition	OA + OY	287	6–11	132–200	[39]
			OA	285	7–35	—	[40]
			HDAHCl-OY	180	15	164	[20]
	Fe(oleate)$_3$	thermodecomposition	OA + NaOA	310	16	101	[41]
	(Fe(N(Si(CH$_3$)$_3$)$_2$)$_2$)$_2$	reduction—H$_2$	PA + HDA	150	1–30	212	[42]
			LA + DDA	150	30–80	210	[29]
	Fe(C$_5$H$_5$)(C$_6$H$_7$)	reduction—H$_2$	OA	130	16	140	[19]
	FeCl$_2$	reduction—LiEt$_3$BH	PMMA	20	5–25	85–184	[43]
		reduction—NaBH$_4$	PEG	20	10	70	[18]
Co	Co$_2$(CO)$_8$	thermodecomposition	OA + TOPO	180	10–16	—	[44]
	CoCl$_2$	reduction—LiEt$_3$BH	OA + TOP	200	2–11	—	[45]
	Co(laurate)$_2$	polyol	—	170	10 × 100	113	[46]
	Co(N(Si(CH$_3$)$_3$)$_2$)$_2$(thf)	reduction—H$_2$	LA + HDA	150	13,7	—	[47]
	Co(η$_3$-C$_8$H$_{13}$)(η$_4$-C$_8$H$_{12}$)	reduction—H$_2$	SA + HDA	150	9 × 40	142	[48]
FeCo	Co$_2$(CO)$_8$ + Fe(CO)$_5$	thermodecomposition	OY	160–250	11	212	[49]
		interdiffusion Co/Fe	OA + OY + DOA		11	192	[50]
	Co(η$_3$-C$_8$H$_{13}$)(η$_4$-C$_8$H$_{12}$) + Fe(CO)$_5$	thermodecomposition + reduction—H$_2$	OA + SA + HDA	150–500	15	220	[51]
	Co(acac)$_2$ + Fe(acac)$_3$	reduction—H$_2$ Diol	OA + OY	300	20	207	[52]
FePt	Pt(acac)$_2$ + Fe(CO)$_5$	thermodecomposition + reduction Diol	OA + OY	297	6	—	[53]
	Pt(acac)$_2$ + Fe(acac)$_3$	polyol	HDD	295	2	—	[54]
	Pt(acac)$_2$ + FeCl$_2$	reduction—LiBEt$_3$H	OA + OY	263	4	75	[55]
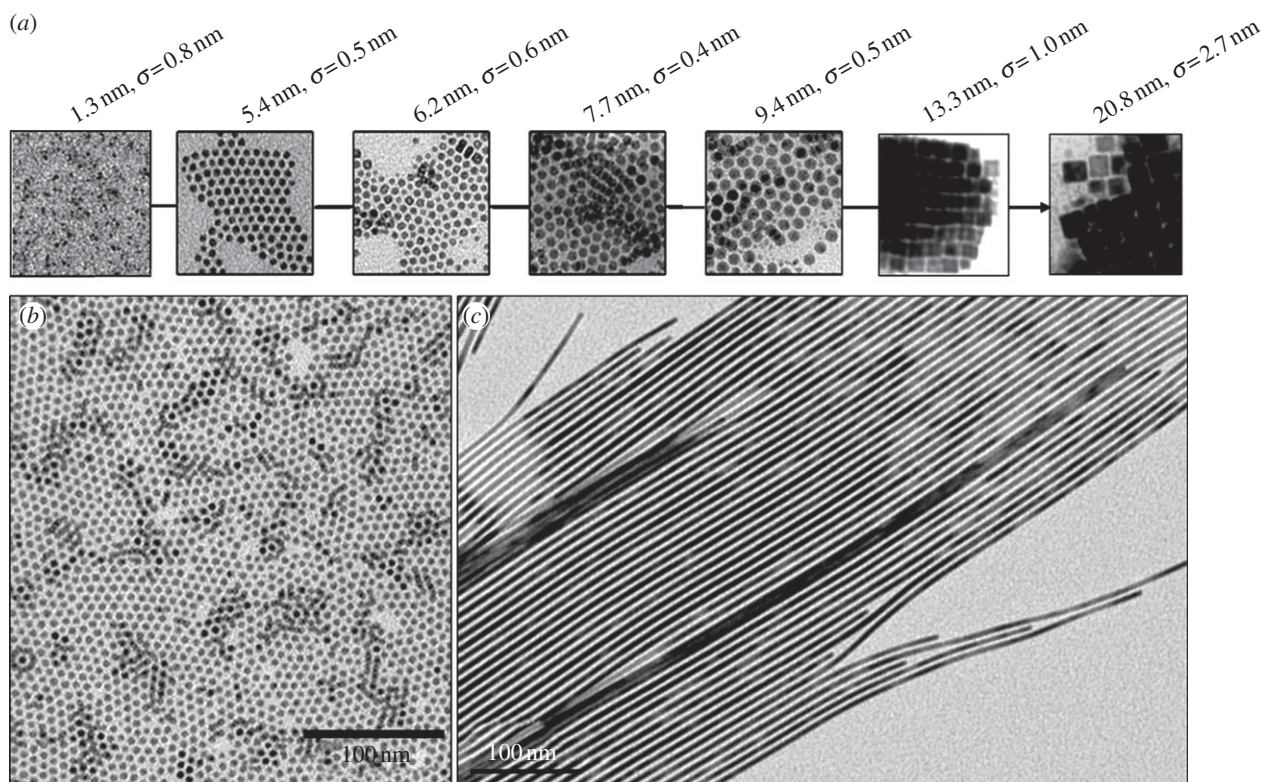
Figure 4. Transmission electron microscope (TEM) micrographs of (*a,b*) Fe NPs with tuneable mean size. (Reproduced with permission from [61].) (*c*) Co nanorods obtained by decomposition under H_2. (Reproduced with permission from [47].) Copyright © 2012 American Chemical Society.

could be prepared. However, the synthesis has been very challenging because of the difference in reactivity of Fe and Co precursors, yielding a core-shell structure (Co@Fe) with reduced magnetic properties [51]. In order to favour the inter-diffusion of Fe and Co, annealing treatments (from 250°C [49,50] to 500°C [51]) were performed, yielding bcc-FeCo NPs with saturation magnetization up to 220 emu/g_{FeCo} [51]. Though chemically prepared FeCo NPs have never been tested for MRI purposes, high T_1 and T_2 relaxivities without any obvious cytotoxicity could be expected as reported for bcc-FeCo NPs prepared via an arc-discharge method [22]. Lately, Pt-based alloys (FePt and CoPt) have also been investigated for biomedical applications. Initially developed for magnetic recording purposes due to the high magnetic anisotropy of tetragonally ordered structures (L_10-phase) [53], FePt combines an enhanced magnetization compared with iron oxides (125 emu/g_{FePt} [64]) and a high cytotoxicity, making them potent anti-cancer drug due to the leaching of Pt ions in biological condition [65].

4. Near-infrared detection principle and near-infrared luminescent semiconductor nanocrystals

In this section, we will first present the basis of NIR imaging and in particular the relevancy (i) of the NIR wavelength window for a high signal to background ratio (thanks to the high transmissivity of the organic tissue in this range of wavelengths) and (ii) of the QDs compared with other fluorescent probes. Then, we will focus on the existing synthetic routes with an emphasis on the development of non-toxic semiconductor nanocrystals (NCs) as an alternative to Cd-, Pb- and Hg-based QDs. These approaches will be examined

in the context of preparing NCs well suited for *in vivo* imaging, i.e. (i) small size to facilitate circulation and clearance and (ii) narrow-size distribution and brightness to provide efficient detection at QDs concentration as low as possible.

4.1. Basics of near-infrared luminescence imaging
4.1.1. Context

Among the various modalities for bioimaging, fluorescence imaging is of special interest because of its low-cost, high-sensitivity, high-spatial resolution and ease to implement (just with a low-light camera). In the case of real-time *in vivo* detection, the fundamental barriers to fluorescence imaging of a tissue are auto-fluorescence, high light scattering and absorption of the different tissue and blood components: water, haemoglobin, melanin, proteins, etc. (figure 5) [66].

These endogenous absorbers possess high absorption characteristics between 200 and 650 nm and thus prevent light penetrating deep into the tissues in the visible range. Moreover, the tissue auto-fluorescence also limits the signal-to-background ratio and hampers the detection of the fluorescent imaging agent. These intrinsic limitations have stimulated, in the last few years, the development of fluorescent probes with absorption and emission maxima in the 650–1450 nm range, where tissues have minimal absorbance and fluorescence [66–68].

As a general guideline, ideal fluorescent probes should also fulfil the following requirements [69]:

— stability in biological media;
— long fluorescence lifetimes for an efficient temporal discrimination from scattered excitation light;
— high brightness (product of high quantum yield, i.e. high number of emitted photons per number of absorbed photons and high extinction coefficient);
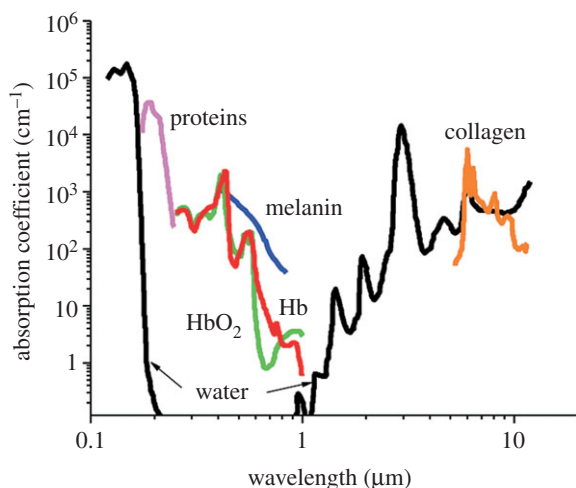
Figure 5. Absorbance of various tissue and blood components from 200 nm to 10 μm. (Reproduced with permission from [66]. Copyright © 2012 American Chemical Society.)

— narrow, symmetric emission bands and large Stokes shifts to easily separate the excitation and emission; and
— no toxicity or interference with cell physiology.

The organic fluorescent dyes (cyanines, pyrroles- or porphyrins-based cycles, squaraines and borondipyrromethene classes) [66], which were historically first used in NIR biodetection [70], are far from ideal probes. In the far-red/NIR wavelength range, they suffer from rather low quantum yield, photobleaching (making them unsuitable for extended periods of observation) and broad emission spectra, which create overlapping detection ranges (inadequate for simultaneous multi-colour applications) [66,71]. Even if remarkable progress has been made to improve the performance of dye-doped silica NPs and to develop new probes such as up-converting NPs [72,73] or noble metal (gold and silver) nanoclusters [5,74], the optical performances (especially QYs) are not yet competitive enough.

Among the NIR fluorescent probes [5], QDs offer currently the best optical properties and appear as a very powerful and essential tool in biodetection. Indeed, they exhibit large molar extinction coefficients, high QY (greater than 50%), narrow and symmetric photoluminescence (PL) emission bands, size-tunable emission and absorption spectra, large two-photon action cross section and high photostability [69]. However, QDs suffer from the drawback of blinking (intermittence in light emission), which is problematic in the case of single molecule tracking [75], instability of QY in different media and possible emission variability due to slight size modification between chemical batches.

4.1.2. Quantum dots specificities
Owing to their nanoscale dimension, the intrinsic physical characteristics of the material are transformed by quantum effects below a certain size limit (Bohr radius), which ranges approximately from 2 to 50 nm according to the material [76]. At these sizes, NCs lie in between the atomic and molecular limit (discrete density of electronic levels) and the extended crystalline limit (continuous bands, i.e. the valence band and the conduction band) of bulk

semiconductors. This leads to size-dependent optical properties (figure 6) [78], the maximum emission wavelength attainable being that of the bulk material.

When NCs are excited by quanta of energy, an electron is promoted from the valence band into the conduction band, leaving a hole in the valence band (electron-hole pair, i.e. exciton generation). The exciton recombination results in light emission at a wavelength longer than the absorbed light (Stokes shift). Several factors can be used to vary band gap and, thus, to control absorption and luminescence wavelengths of the NCs. Classically, band gap engineering can be achieved through the variation of (i) the particle size, or (ii) of the composition. Several alternatives exist for modifying the band gap: (iii) doping the semiconductor host NCs with the incorporation of small amount of impurities, and (iv) modifying the internal structure (homogeneous versus graded), for example, in ternary system QDs like $CdSe_{1-x}Te_x$ [79]. Thanks to these strategies, there are now a large variety of QDs that luminesce in the NIR region as illustrated in figure 7.

Finally, one can find a last strategy for designing NIR-emitting QDs that is based on core/shell (C/S) architecture: the core and shell are rationally chosen in order to favour the relaxation of a conduction band electron of the core into the valence band of the shell (type II QDs; figure 9c) [102]. The staggered band alignment leads to a smaller effective band gap than each one of the constituting core and shell materials. This aspect will be described in more detail in §5.1 devoted to heteronanocrystal, i.e. NCs incorporating two or more materials organized in C/S or core/multi-shell architecture.

4.2. Luminescent semiconductor nanocrystals: chemical synthesis of NIR-emitting core nanocrystals
The literature reports a large variety of Cd-, Pb- or Hg-based QDs for which the synthetic routes can be generally classified in two families, according the synthetic medium (aqueous or not). Different protocols have been described in water to produce II–VI semiconductors, such as CdTe, $CdSe_xTe_{1-x}$, HgTe, $Cd_xHg_{1-x}Te$ or $Cd_xHg_{1-x}Se$ QDs [103]. The major advantages of this aqueous medium approach are (i) the environmentally friendly medium, (ii) the ease to scale up to gram scale amounts for commercial purpose and (iii) the aqueous compatibility for applications, in particular biomedical imaging [104]. However, the size distribution is often broad and post-preparative procedures (size-selective precipitation) are required [80].

In this context, the development of the alternative hot-injection method, i.e. the synthesis of NCs in high-temperature boiling organic solvents is considered as one of the main milestones in the chemistry of QDs. The temporal separation of the nucleation and the growth of the seeds gave access to high-quality NCs with narrow-size distribution (5–10% s.d.) without laborious size-selective precipitation procedure. Since the first published articles (Murray *et al.* [105] for CdE (E = S, Se, Te)), synthetic improvements have allowed an ongoing trend towards simpler and safer procedures (replacement of the hazardous [106] or expensive chemicals [107], decrease in reaction temperature to approx. 100°C [108]). Moreover, the widespread success of the hot-injection strategy is also largely because of its versatility, in particular in terms of chemical variety. The extension of the list of semiconductor
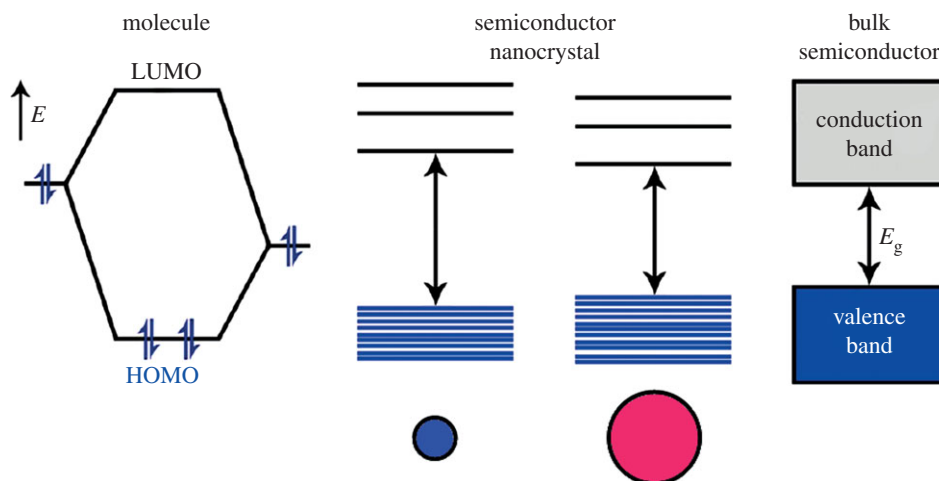
Figure 6. Electronic energy states of a semiconductor in the transition from discrete molecules to nanosized crystals and bulk crystals. Shading denotes ground-state electron occupation. (Adapted from [77]. Copyright © 2012 American Chemical Society.) (Online version in colour.)
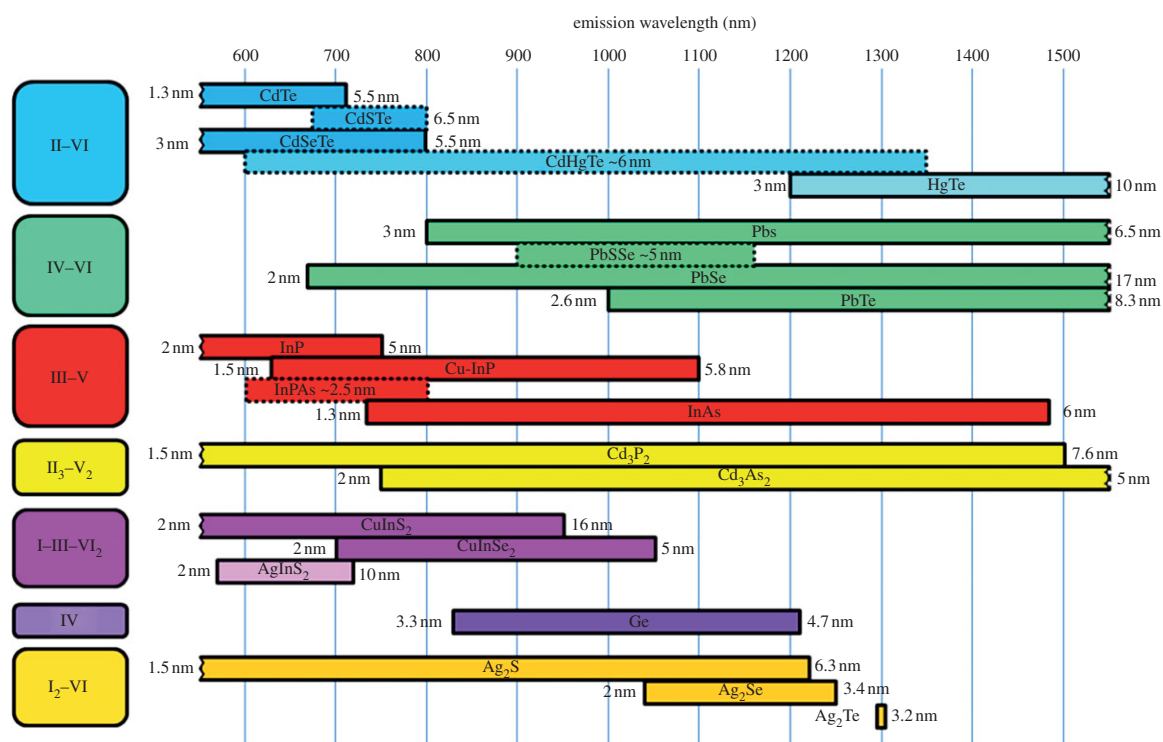

Figure 7. Composition, size and wavelength ranges of reported NIR-emitting QDs prepared via solution-based methodologies. Emission wavelengths reported for constant size NCs containing different proportions of elements are represented with broken lines rectangle. The references used for the figure are the following: II−VI [79−84], IV−VI [85−89], III−V [90−93], II$_3$−V$_2$ [94,95], I−III−VI$_2$ [96,97], IV [98,99] and I$_2$−VI [100,101]. (Online version in colour.)

materials to high quality (in terms of monodispersity and optical emission) IV−VI QDs such as PbE (E = S [86], Se [109], Te [110]) is one of the valuable consequences [111]. Finally, emerging materials such as II$_3$−V$_2$ are also worth citing: for instance, a room temperature procedure has recently been developed to yield Cd$_3$P$_2$ QDs that emit in the NIR region [112] and can be envisioned for biodetection. It should also be noted that in case of mercury-based NCs, the aqueous strategy remains the best-suited and almost exclusive approach [103,111].

In the context of *in vivo* applications, the issue of metabolic clearance is still an open and unresolved question. To avoid any dilemma, one strategy is to extend the NC family towards more environmentally friendly elements than Cd, Pb or Hg [113]. We have chosen to detail this attractive perspective in §4.2.1, 4.2.2 and 4.2.3.

4.2.1. Synthesis of Pb-free IV−VI semiconductors nanocrystals (GeE, SnE, E = S, Se, Te)

While the use of precisely controlled reaction conditions (air- and water-free atmosphere) can be seen as a major drawback when aiming at simple and straightforward procedures, these requirements offer, on the other hand, the opportunity to

introduce novel precursors yielding unexplored materials for NCs, such as the tin and germanium chalcogenides [114]. The preparation of SnTe NCs [115] using the sophisticated tin complex bis[bis(trimethylsilyl)amino]tin(II) (Sn[N(SiMe$_3$)$_2$]$_2$) and trioctylphosphine telluride was the starting shot towards materials involving these lighter elements of the Pb group. Today, a large variety of compositions (GeS, GeSe, GeTe, Ge$_x$Sn$_{1-x}$Se, SnS$_x$Se$_{1-x}$, etc.) and morphology (sphere, sheet and needle) with tunable band gap in the NIR region is accessible [114]. Although the emission properties have not yet been explored, tin and germanium monochalcogenide represent very promising materials which deserve to be tested in the context of biodetection.

4.2.2. Synthesis of III–V semiconductors nanocrystals (InP and InAs)

Following the same tendency towards 'greener' material, III–V semiconductors are generally viewed as a highly relevant alternative. This is in particular the case for InP NCs which have been rapidly identified as one of the most promising alternatives to Cd- and Pb-based QDs and have been the focus of the majority of the research efforts devoted to III–V QDs. InP NCs were first prepared in 1994 [116] following, at the time recently published, the hot-injection procedure developed for CdE (E = S, Se, Te) QDs with indium oxalate and tris(trimethylsilyl)phosphine (P(SiMe$_3$)$_3$). Longer reaction times (3–7 days) were required to yield good cristallinity. The progress towards easy, reliable and controlled synthesis (i.e. in non-coordinating solvent) followed that of their II–VI analogues [117], but remains one step behind, particularly for the size control. The preparation of QDs larger than 5 nm is still a challenging question. This issue is of central importance because absorption wavelengths higher to 650 nm are at the upper limit of the current attainable range with InP [90]. It has recently been shown that the formation of a mixed oxide shell InPO$_x$ at the surface of the NCs is probably the reason of this growth inhibition. This is a consequence of the oxophilic character of phosphorus and of a side reaction of the carboxylate ligand occurring at the temperature (230°C–300°C) required for the formation of NCs, which generates oxidative conditions in the reaction medium [118]. However, the doping strategy proved to be successful and allow emission wavelengths up to 1100 nm to be reached [91]. InAs NCs were also prepared following the hot-injection method, usually by the reaction of As(SiMe$_3$)$_3$ and indium chloride [119] or acetate [117]. In the latter case, the QD size can be controlled to access a range of emission wavelengths well suited for biodetection purposes, i.e. between 700 and 1400 nm, with diameters approximately less than 6 nm [93]. As an example, InAs NPs of 3.2 nm diameter emitting at 750 nm can be easily cleared from the body [120].

4.2.3. Other semiconductors (IV, I$_2$–VI and I–III–VI$_2$ types) for NIR-emitting nanocrystals

Over the last decade, significant progress has been made concerning the chemistry of NCs of materials as alternatives to II–VI, IV–VI and III–V. So far, two main families have been the focus of the majority of research efforts: elemental group IV (Si, Ge) semiconductors and I–III–VI$_2$ chalcopyrite types such as CuInE$_2$ (E = S, Se) or AgInS$_2$ [96]. In the latter case, the synthetic strategy is essentially the same as the one developed for the hot-injection method for II–VI, IV–VI and III–V materials, i.e. in coordinating (TOPO) [121] or non-

coordinating (dioctylphtalate [122], ODE [123]) solvents. Concerning group IV element NCs, the synthesis is far less developed. Two main solution strategies exist and involve either strong reducing agents (zintl salts, LiAlH$_4$, K/Na alloy) and/or high-temperature procedures (usually supercritical thermolysis condition) [98]. An exception to this rule are the approaches developed by the Boyle [124] and Klimov [99] groups, who took advantage of the reactivity of Ge(II) precursors using hot-injection approach. Very recently, silver chalcogenide Ag2E [101] and in particular silver sulfide Ag$_2$S [125] were identified as promising materials for NIR-emitting QDs. For these NCs, both aqueous [100,126,127] and organic [101,125,128] solvent approaches were developed with similar results in terms of size distribution and optical quality, which opens the way for *in vivo* studies [100,126].

5. Surface modification and probe development

In view of their applications for biological imaging, NPs cannot be use directly after their synthesis for two major reasons. First, because nano-objects have high surface to volume ratios, a large fraction of the constituent atoms are located on the surface. These atoms are incompletely bonded within the crystal lattice, thus disrupting the crystalline periodicity and leaving one or more 'dangling orbital' on each atom pointed outward from the crystal. While partially stabilized through dative ligand–metal bonds, the organic passivation is generally insufficient to provide inertness to the biological medium and/or to air. These surface atoms, indeed, remain highly reactive and are usually prone to oxidation. A general strategy to improve NPs' surface passivation is the overgrowth of a protecting shell around the core, affording chemical stability and preservation of the physical properties. A second requirement aiming at exploiting the magnetic or luminescent properties for biodetection is the solubility of the NPs in physiological media. As discussed in the previous sections, the NPs of best quality are generally produced in non-polar solutions using aliphatic coordinating ligand making them insoluble in water. In this context, the phase transfer is an essential but non-trivial step before envisioning their use for biodetection. Finally, the surface of these water-soluble C/S NPs often needs to be engineered for *in vivo* applications in order to increase the circulation time in the blood stream and enhance their targeting efficiency. The final object is then composed (as depicted in figure 8) of an inorganic core with optimized physical properties, surrounded by an inorganic shell and an organic corona composed of hydrophilic ligands and targeting molecules.

5.1. Coating the active core
5.1.1. Magnetic nanoparticles
Contrarily to iron oxide- and ferrite-based NPs, metallic NPs, which exhibit optimized magnetic properties, are highly reactive towards oxidation. Under air exposure, drastic decrease in the magnetization was reported for Fe [20,129] and FeCo NPs [51]. Under acidic environment, as encountered by NPs during cell uptake within lysosomes, metallic core disintegrates releasing M^{n+} ions [130] or $M^{\bullet}$ radicals [131], which can lead to the apoptosis of the host cells [130]. Therefore, the outgrowth of a passivating shell is a mandatory step prior to the use of metallic NPs as optimized contrast agents for MRI.
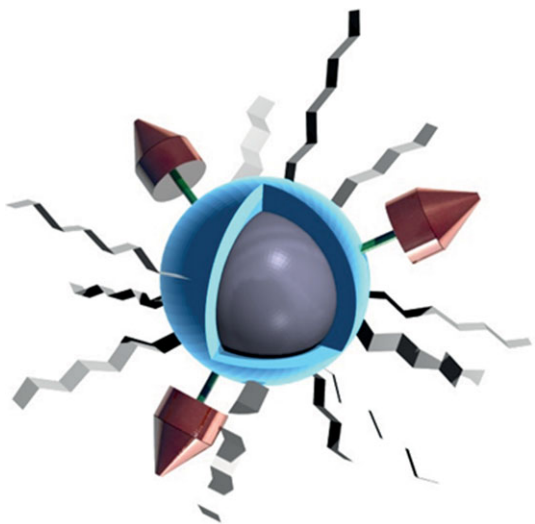
Figure 8. Schematic of a surface engineered active core (grey) coated with an inorganic shell (blue), hydrophilic surfactants (light grey) and targeting agents (red).

Owing to its inertness and its low toxicity [132], gold would be a perfect candidate for such a protective shell. Though promising results have been reported through the transmetallation process [133], the chemical growth of a continuous shell on pre-formed metallic NPs is challenging, as recently reviewed [134]. Self nucleation of gold yields hybrid objects composed of metallic NPs decorated with small Au islands [135]. Thus, multi-step physical approaches (lithographic process, multiple metal evaporations), though time consuming, have so far been preferred for Co@Au NPs tested for MRI [21].

Oxide shells are alternative candidates that benefit from (i) fairly low toxicity levels [136] and (ii) simple chemical strategies. The simplest choice relies on the oxide shell which naturally grows at the surface of the metallic core exposed in air. For instance, the native CoO shell is an efficient passivating layer for a Co core. In the case of Fe, the stability of Fe@Fe_3O_4 requires a crystalline oxide shell [129]. While such a shell is naturally obtained on a single crystalline Fe core [20] a controlled oxidation process at high temperature is required for amorphous Fe core [129]. Though CoO and crystalline Fe_3O_4 confer air-stability, these shells are stable in aqueous media only in a selected pH and ionic strength range. Therefore, the SiO_2 coating, owing to its remarkable stability in water, has been extensively studied [137]. Silica coating is often grown through water-in-oil microemulsion which may induce oxidation of the metallic core, thus alternative approaches based on non-alcoholic solvents should be preferred [138,139]. Additionally, silica shell grown in liquid phase is generally not fully condensed (incomplete hydrolysis and condensation steps). Thus, post-treatments (annealing as example) are required to make it denser and to prevent a possible permeation to oxygen or any leaching of metallic ions from the core. To the best of our knowledge, such M@SiO_2 NPs (M = metal) with a well-condensed shell have not been tested so far *in vitro* or *in vivo*.

Finally, a graphitic shell can also be grown to stabilize a metallic core either through the calcination of the surrounding ligands [51] or through chemical vapour deposition [22]. Such a shell has the advantages of being thin, functionalizable and, to date, no negative health problems have been detected [22].

However, coating of highly reactive Fe NPs should be tested to decide on the efficiency of such C shells towards oxidation.

5.1.2. Quantum dots

In the case of QDs, the role of the shell goes well beyond the sole function of protecting against oxidation and photo-oxidation. The dangling orbitals of the under-coordinated atoms located at the surface may form energy states ('surface energy state'), which quench luminescence through non-radiative decay paths (figure 9*a*) [77]. When coating, the dangling bonds are passivated with atoms of the shell, resulting in the dramatic enhancement of the PL efficiency. As an example, the QY of naked InP NCs is generally inferior to 0.1 per cent but after being coated with ZnS, the QY of the resulting InP/ZnS C/S QDs increases up to 22 per cent [141]. In the majority of cases, the materials chosen for the shell are semiconductors which have a wider band gap than those of the core (C/S system called type I structure) in order to provide electronic insulation thanks to the confinement of both electrons and holes in the core (figure 9*b*). A representative (but not exhaustive) list of commonly encountered compositions for NIR-emitting C/S NCs is CdTe/MS (M = Zn, Cd), HgTe/CdS, PbSe/PbS, PbSe/CdSe, InP/ZnE (E = S, Se), InAs/InP, InAs/GaAs, InAs/CdSe, Cd_3P_2/ZnS, CuInE/ZnS (E = S, Se) [96,102,112]. For bioapplications, the shell is generally composed of non-toxic elements (e.g. ZnS, prepared with zinc stearate and dodecanethiol) to minimize potential toxic effects by preventing the leaching of elements from the core [102]. A general requirement for obtaining highly luminescent C/S QDs is the epitaxial growth of the shell and, thus, the use of a material which crystallizes in the same structure as that of the core and has small lattice mismatch with it [142]. The shelling of the QDs is achieved through the slow addition (in order to avoid side-nucleation and formation of separate NCs composed of the shell materials) of the shell precursors into a solution of the purified core. An example of this kind of C/S architecture is $InAs_xP_{1-x}$/InP/ZnSe alloyed QDs for which ZnSe was chosen for its better lattice match to InP than ZnS [92].

Interestingly, by choosing the appropriate shell material, it is possible to tune the emission at wavelengths that cannot be achieved with either of the two materials (those of core and shell) alone. In this type II system, both the valence and the conduction bands of the shell are lower (or higher) than in the core. As a consequence, this band alignment leads to a smaller effective band gap than either the core or the shell material (figure 9*c*). This approach is particularly relevant for attaining the NIR window: for instance, the emission wavelength of the CdTe/CdSe and CdSe/ZnTe C/S heterostructures could be tuned in the NIR range, while these emission wavelengths would not be reached by increasing the size of the respective CdTe or CdSe cores [143]. In general, type II C/S QDs have low QY and low photochemical stabilities because one charge (either the electron or the hole) localized in the shell is in direct contact with the surrounding medium and, thus, similar reactions to those of naked QDs may occur [134]. These two properties can be improved by coating with another semiconductor material to yield a core multi-shell structure [102].

Last, blinking of QDs which is highly detrimental to their use for single molecule tracking [75] can be suppressed by coating with thick shells (i.e. 20 monolayers) yielding a final diameter of approximately 15 nm [144]. The major
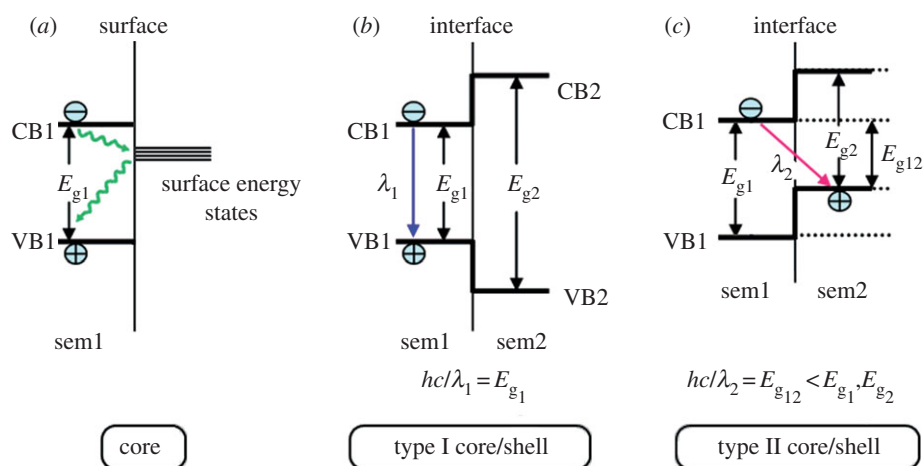
Figure 9. Core (*a*) type I, (*b*) and type II core-shell, (*c*) band edge alignments at the surface and the heterointerface between two semiconductors. In the type I structure, both the electron and the hole localize within the material with a narrower energy gap, which is semiconductor 1 (sem1) in the present case. As a result, the wavelength emission, λ_1, is determined by E_{g1}. The energy gradient existing in the type II structure tends to spatially separate the electron and the hole on different sides of the heterointerface. In this case, the wavelength emission λ_2 is determined by the energy difference between the conduction band edge of sem1 and the valence band edge of semiconductor 2 (sem2), and hence, it is lower than the band gap of either semiconductor. (Adapted from [140]. Copyright © 2012 American Chemical Society.) (Online version in colour.)
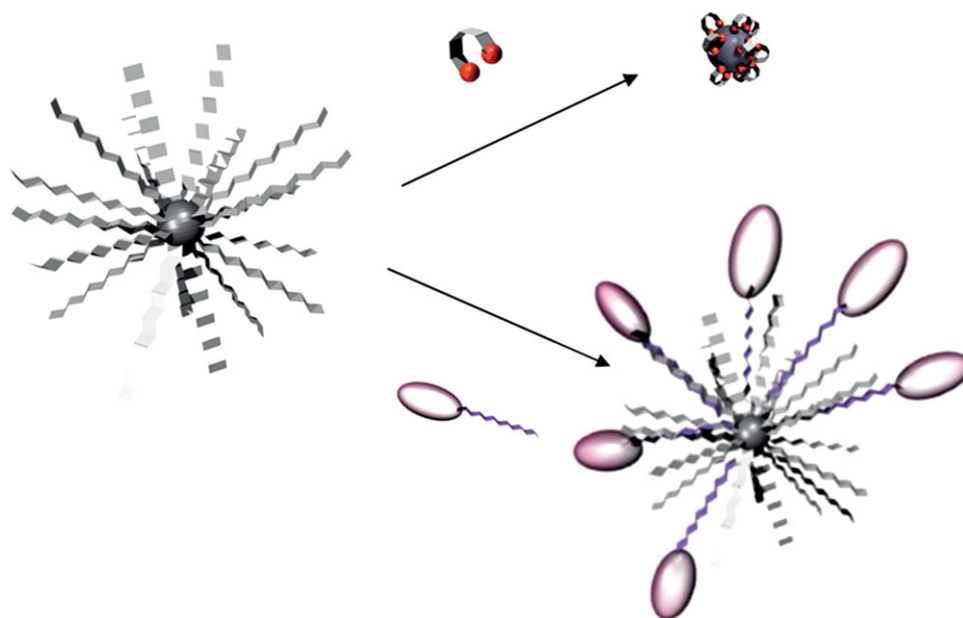

Figure 10. Schematic of the three generic strategies for water transfer of hydrophobic NPs: through ligand exchange or copolymer addition. (Online version in colour.)

drawback is the large size, which may be inappropriate for the observation of molecular phenomenon [75], but this problem has been shown to be possibly circumvented when a composition-graded interface exists between the core and the shell in the more compact (8 nm) CdSe/ZnSe QDs [145].

5.2. Phase transfer and surface modification
5.2.1. Phase transfer, water stability, stealth
Phase transfer becomes an important issue once optimized functional NPs have been prepared in organic solvent; different strategies have already been reviewed [146,147] and can be divided, in a first approximation, between two generic approaches (figure 10):

— ligand exchange: hydrophobic surfactants are replaced by a bifunctional ligand presenting at one end, a function holding a stronger affinity with the NP surface than the initial ligand and, at the other side, a hydrophilic ending. To enhance the binding affinity and favour a complete replacement of the hydrophobic surfactants, polydendate ligands, such as dimercaptosuccinic acid (DMSA), are often used [16]. This ligand exchange approach is particularly useful to stabilize water-soluble NPs with small hydrodynamic size (less than 20 nm), but may lead to particle aggregation and loss of optical properties for QDs [147]. This problem is commonly encountered for C/S QDs such as CdSe/ZnS [148]. InP/ZnS [149] or the other NIR-emitting material CuInS$_2$/ZnS [150]. Recently, Reiss and co-workers [150] have given insight on the precise mechanism, attributing the quenching to hole transfer from the QDs to the capping ligand (cysteine) resulting in the formation of the cysteine dimer (cystine); and

— copolymer addition: amphiphilic surfactants are added, their hydrophobic tails form weak interactions with the existing hydrophobic coating while their hydrophilic

groups are exposed, ensuring water-solubility. A variety of lipophilic polyethylene glycol (PEG)-based polymers has been used [147]. Such copolymer strategy leads to a drastic increase in the hydrodynamic size of the NPs (greater than 20 nm) but ensures fairly long blood circulation due to PEG moities [151].

The choice of functionalization strategy results from a delicate balance between the surface state chemistry of the NPs and the final hydrodynamic diameter reached. Hydrodynamic size influences the relaxivity constant and drives the interactions with tissues and biological media (through size-dependent diffusion). While ultra-small particles (*ca* 5 nm) are quickly excreted by the kidney, intermediate NPs (15–100 nm) exhibit longer circulation time [152], larger NPs (greater than 100 nm) being more susceptible to opsonization (uptake by the immune defence system). Thus, the functionalization strategy must be carefully chosen in order to reach the optimized window of hydrodynamic size (15–100 nm).

In addition to the hydrodynamic size effect, the pharmacokinetics and biodistribution of NPs is driven by surface coating. Lifetime in blood circulation strongly depends on the interaction of the NPs with plasma proteins (opsonins). Accumulations of opsonins are recognized by the reticuloendothelial system, and phagocytosis by macrophage grafting of PEG on the surface of NPs may inhibit protein interaction and prolong blood circulation time [153]. This effect strongly depends on the conformation of the PEG chains at the NPs surface, which evolves from mushroom to brush configurations for longer PEG chain (greater than or equal to 2000 Da) and higher surface density [153]. While brush configurations generate greater protein repulsion, it may also lower the NP targeting efficiency due to steric shielding of the specific agents [154]. Therefore, targeting agents should be conjugated to a PEG-spacer of similar length to stand at the outmost exterior of the NPs, lying above the organic corona [153].

5.2.2. Cancer cell targeting
Numerous reports have shown that most NPs accumulate in tumours due to enhanced permeation and retention (EPR) effect, which results from relatively large and permeable blood vessels along with poor lymphatic drainage of tumour cells [153]. For instance, iron oxide NPs were successfully used to diagnose cancer without any targeting agents [155]. Such a cancer cell uptake strategy is referred to as passive targeting and let us consider the possibility of universal labelling. Charged NPs have been tested for universal labelling but controversial results have been found. While anionic NPs (citrate) have been reported as exhibiting a better cell uptake than cationic or uncharged NPs [156], another study shows that cationic (aminodextran) NPs were optimized [157]. Though contradictory, these results might be explained by the tendency of charged NPs to be destabilized under harsh pH and ionic strength environments, as encountered in biological media.

In order to enhance the selective internalization of NPs, active targeting strategies were developed. Driven to the vicinity of tumour cells by EPR effect, NP grafted with adequate moieties would be internalized faster through receptor-mediated endocytosis. Such tumour surrounding

clearance generates a diffusion gradient which can favour further NP flow, and, thus, the accumulation of NP within the tumour region [153]. One of the main challenges of active targeting is the design of adequate targeting moieties. Indeed, tumour cells exhibit receptors fairly similar to the surrounding healthy cells, the difference being their relative abundance. Therefore, targeting agents must specifically bind to overexpressed receptors. Small molecules, peptides, proteins, aptamers and antibodies have demonstrated high affinity with receptors overexpressed in malignant cells as previously reviewed [2,30,153]. A key issue during the grafting of such moieties onto the NP surface is to maintain their affinity for receptors. Their density, accessibility and conformation should be preserved; thus, spacers are often added to avoid shielding and denaturing of the ligand.

6. Applications
In this part, we aim to illustrate the recent progress in MRI and NIR *in vivo* real-time imaging due to the use of the new generation of magnetic NPs and QDs. The last part will aim to present the recent very first attempts to combine of both properties in multi-modal single nano-objects and the promises of this strategy.

6.1. Magnetic resonance imaging *in vivo*
In this part, we aim to illustrate the recent progress in *in vivo* MRI due to the use of the new generation of magnetic NPs. The main objective is to evaluate the potentialities of the latter to favour further developments in this field of application. Reviews on MRI using 'classical' MNPs (SPIO and USPIO) can be referred to for comparison purposes; they generally describe *in vivo* MRI experiments dealing with cancer, cardiovascular disease or molecular imaging [158]. Here, we only report examples of MRI improvements due to new contrast agents. Moreover, we would like to mention studies that directly compare MNPs whose magnetic materials were of different nature, but coating and functionalization were identical. This way, the other parameters that necessarily impact the MRI response (coating thickness, bio-distribution, etc.) can be considered unchanged.

As previously explained, the main reason for working on magnetic composition of contrast agents is to enhance contrast on MR images. In a recent study reported by Cheong *et al.* [19], it was shown that Fe/FeOx core/shell NPs improve by a factor 2 the contrast in T_2-weighted MR images of mice nodes compared with pure FeOx NPs. Interestingly, they allow for a much better *in vivo* detection of small tumours (1–3 mm) at 1.5 T [19]. *In vivo* probing of small cancers (approx. 50 mg) with manganese ferrite NPs coated with DMSA and conjugated with the cancer-targeting antibody Herceptin was also successful, as reported by Cheon's group [16]. In contrast, the analogue pure iron oxide NPs did not allow such performances. The authors attribute this promising result to the higher saturation magnetization of the manganese ferrite NPs. Developed by Chen *et al.*, the 12 nm FePt NPs conjugated to the anti-Her2 monoclonal antibody showed significant contrast enhancement in both MRI and CT, thus taking advantage of their magnetic properties and the high X-ray absorption of platinum [159]. Indeed, 24 h after injection (28 mM Fe concentration, 100 μl) into mice bearing transplanted MBT2
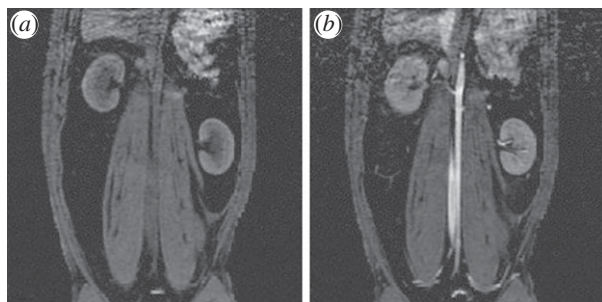
Figure 11. T_1-weighted MR images of a rabbit (a) before and (b) 30 min after initial Injection of a solution of 4 nm FeCo/GC NCs (metal dose 9.6 μmol kg^{-1} for the 5 kg rabbit). The blood pool in the aorta is significantly brightened (positive contrast) in the MRI after injection. We also see signal increase in the kidney medulla and cortex due to the high blood volume within the kidney. We see little signal enhancement in the muscle. (Reproduced with permission from Macmillan Publishers Ltd: Nature Materials [22]. Copyright © 2006.)
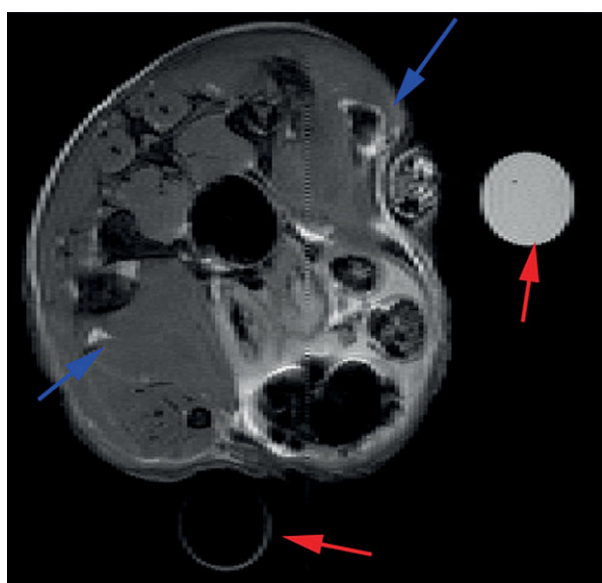

Figure 12. Transverse (axial) MRI image in mouse leg muscle injected with Co nanowontons in PBS solution. The arrows indicate the sites of injection for the nanowontons (upper right corner) and the PBS control (lower left corner). Two water-carrying test tubes are also visible in the scans for purposes of MRI slice alignment (red arrows). MRI parameters were: TE = 50 ms; TR = 1 s; field of view is 2.6 cm × 2.6 cm, and slice thickness is 0.5 mm. (Online version in colour.)

tumours, the MR images showed 51 per cent intensity reduction on the tumour lesion while CT image analysis revealed 138 per cent contrast enhancement. In addition, the biodistribution of the non-functionalized FePt NPs evaluated on mice suggest that they could be cleared from the body after about one week.

The FeCo@graphitic carbon (GC) NCs prepared by Dai and co-workers [22] showed unusually higher r_1 and r_2 values than conventional Gd and iron oxide-based contrast agents. As an example, they allowed for positive contrast enhancement on T_1-weighted MR images of the blood pool in rabbits (figure 11).

This was 30 min after NP injection using a metal dose of only 10 per cent of what was typically used for existing Gd agents (metal dose approx. 9.6 μmol kg^{-1} for the approx. 5 kg rabbit). The authors claim that this represents an

important achievement in MRI contrast-agent development; long-circulating positive contrast enhancement at low metal dosages *in vivo* is indeed particularly interesting for angiographic MR images.

The Co@Au nanowontons reported by Bouchard *et al.* [21] were dual-modality MRI/photoacoustic tomography (PAT) contrast agents. Even when injected in mice muscle leg at a concentration as low as 50 pM, a negative contrast was clearly detected on T_2-weighted spin echo MR images (figure 12). Interestingly, this degree of sensitivity approaches that of radioactive labels. PAT detection was also conclusive as observed for an injection of 100 pM of nanowontons in the tail of a rat.

6.2. Luminescence

Thanks to their remarkable features, NIR-emitting QDs have become one of the mainstays of *in vivo* imaging modalities [160]. This success story started a decade ago with the real-time mapping of sentinel lymph nodes in mouse and pig, using type II C/S CdTe/CdSe QDs [161]. Since this significant achievement, progress has been made in several main domains: biodistribution of QDs, tumour imaging, tracking of cells and vascular imaging (blood vessel and lymphatic circulatory system) [104,160].

Unfortunately, these results have been obtained using toxic elements such as Cd, Pb, Hg or As. The toxicity concerns associated with this family of materials have fuelled research for their replacement with non-toxic elements. The relevancy of these materials (CuInE$_2$/ZnS [97,162–165], InP/ZnS [166], Ag$_2$E [100,126] with E = S, Se) for *in vivo* NIR imaging has been proved in very recent years in the context of biodistribution [163], tumour [162,166] and lymph imaging [97,164]. The lower *in vivo* toxicity of these alternative material QDs has been examined and experimentally confirmed for CuInS$_2$/ZnS and InP/ZnS [164,166].

As a representative example of the potential of such a tool for real-time *in vivo* visualization, Reiss and co-workers [163] monitored the fluorescence distribution of CuInS$_2$/ZnS QDs (functionalized with dihydrolipoic acid yielding a hydrodynamic diameter of approx. 17 nm) with time (figure 13). QDs were injected intravenously into the tail of nude mouse and after 15 min, they accumulate in the liver, spleen and lungs (fluorescence in the stomach is attributed to the feed).

Additionally, Gu and co-workers [162] recently demonstrated for the first time the capability for *in vivo* multiplex imaging, using two different NIR-emitting QDs. A total of 720 nm and 800 nm emitting CuInS$_2$/ZnS NCs were injected into the mouse subcutaneously, respectively, in the right and the left paws (figure 14).

When excited at 660 nm, both types of QDs can be observed while only the fluorescence signal of the left leg remained very bright when irradiation occurs at 766 nm. This result indicates that CuInS$_2$/ZnS QDs could be used for *in vivo* multiplexed molecular imaging by selecting the appropriate excitation wavelength or filter (not shown here) [162].

However, progress differs significantly according to the materials: while being highly promising, the Ag$_2$E-based QDs (E = S, Se) are still in the first stage of development with the proof of principle of *in vivo* NIR fluorescence penetrability [100,126]. In contrast, impressive results were recently reported by Cheng and co-workers [166] with sophisticated biocompatible Dendron-coated InP/ZnS QDs (hydrodynamic diameter approx. 12 nm). These latter results satisfy many of the
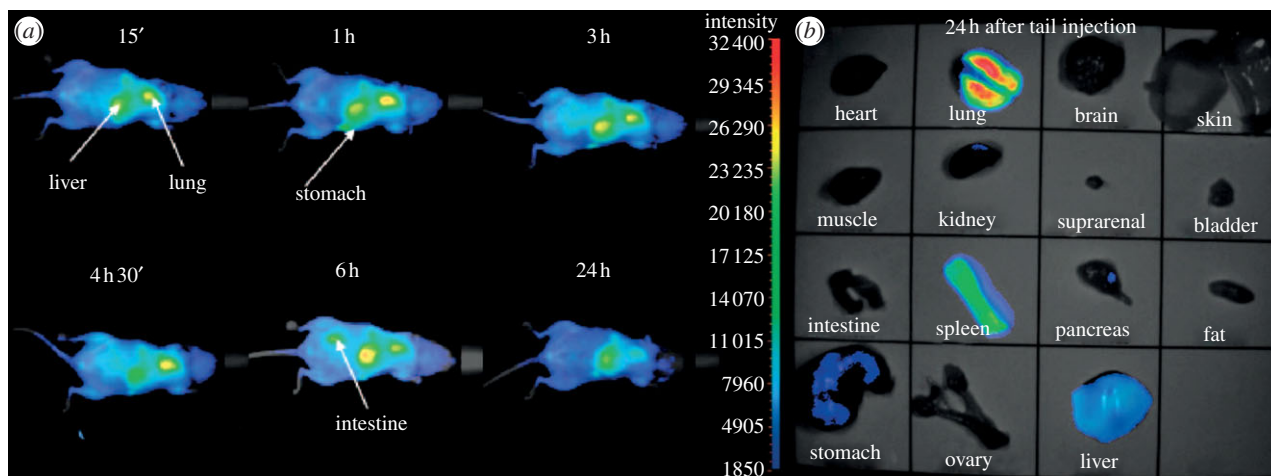
Figure 13. (a) Fluorescence images (excitation wavelength 633 nm) showing the temporal evolution of the biodistribution of the CuInS$_2$/ZnS NCs injected intravenously into the tail of a healthy nude mouse (equiv. 6.5×10^{16} to 1.3×10^{17} copper atoms). The integration time is 200 ms and the contrast has been set between 1850 and 32 400. (b) Fluorescence images of the different parts of the mouse after dissection. (Adapted from [163]. Copyright © 2012 American Chemical Society.)
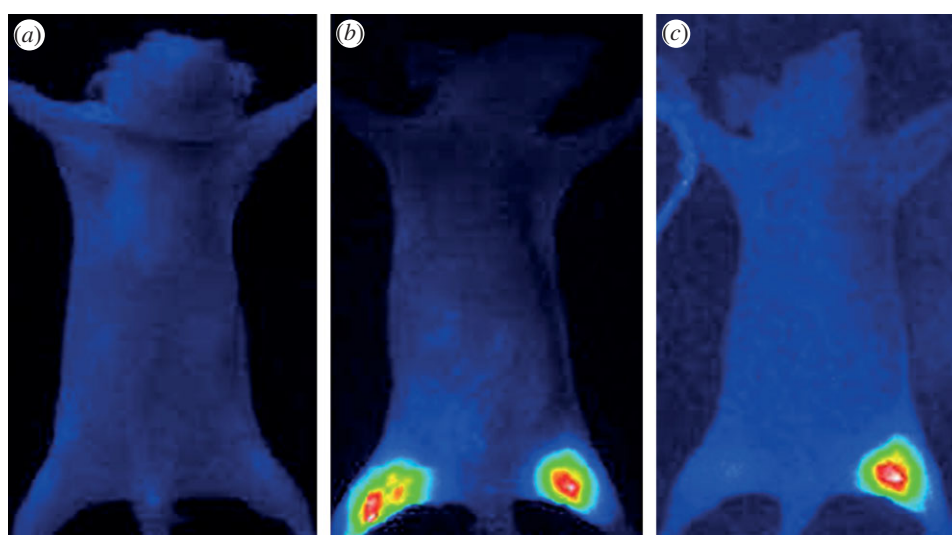

Figure 14. Multiplex NIR fluorescence imaging of mouse administered with two different NIR-emitting QDs-loaded micelles by subcutaneous injection (the right leg, 720 nm-emitting NCs; the left leg, 800 nm emitting NCs): (a) before injection, (b) $\lambda_{ex} = 660$ nm, a 700 nm long pass filter, (c) $\lambda_{ex} = 766$ nm, an 800 nm long pass filter. (Adapted from [162]. Copyright © 2012 American Chemical Society.)
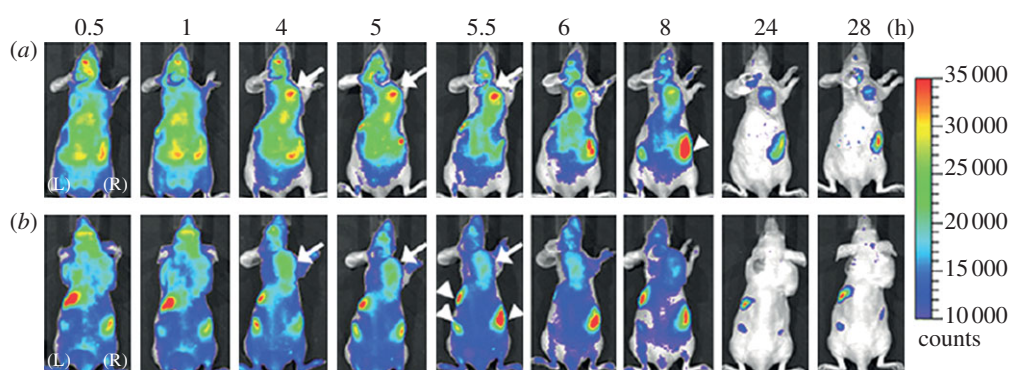

Figure 15. The dorsal images of SKOV3 tumour-bearing (arrows) mice injected with (a) InP/ZnS-Dendron-RGD2 (200 pmol) and (b) InP/ZnS-Dendron (200 pmol) at 0.5, 1, 4, 5, 5.5, 6, 8, 24 and 28 h, respectively. The incidental high fluorescent signals in other body parts (arrowheads) might have originated from regular rodent food in stomach and faeces in intestine. (Reproduced from [166]. Copyright © 2012 American Chemical Society.)

requirements (NIR emission with high efficiency, high stability in biological media, biocompatibility, suitable small size with possible renal clearance, ability of extravasation) for clinical translation. In the article [166], they were used as nanoprobes to

demonstrate *in vivo* the highly specific targeting of Dendron-RGD$_2$ for imaging integrin $\alpha v \beta 3$-positive tumours. The fluorescent signals derived from InP/ZnS NCs functionalized, respectively, with Dendron and Dendron-RGD$_2$ were monitored

in real-time over 28 h (figure 15). Thanks to the high sensitivity of these QDs, the difference of behaviour induced by the different functionalization could be evidenced. In the case of Dendron-RGD$_2$ functionalization, long-term retention is clearly observed from the fluorescence signal at the tumour site (indicated by the arrow, figure 15) which carries on after 28 h. In contrast, tumour uptake of InP/ZnS QDs-Dendron with visible contrast from surrounding tissues can be observed between 4 and 6 h and then disappears. This behaviour was assigned to the enhanced permeability and retention (EPR) effect for the suitably small InP/ZnS QDs-Dendron.

6.3. Multi-modal

Recently, hybrid NPs combining at least two properties have received lots of interest, as shown by the increasing number of dedicated reviews [167,168]. Combining optic and magnetic properties within the same nano-object would open new perspectives towards multi-modal imaging (NIR and MRI) [169], and theranostic applications, coupling detection and treatment potentialities [170]. However, one of the main issues is to keep both physical properties unaltered. QD luminescence can be strongly reduced due to electron transfer and competitive light absorption with the magnetic material. The direct growth of QD onto magnetic NPs, forming FePt-QDs heterodimers [171] or FePt@CdSe core/shell structure [172], results in a prominent quenching of the fluorescence [173]. Analogously, the growth of Co tips onto preformed CdSe nanorods results in an emission intensity 30 times lower than that of pure CdSe rods [174].

To prevent electron transfer, which results in luminescence quenching, QD and magnetic material could be isolated. One strategy is based on the use of metal oxide, insulating material, as the magnetic component of the heterodimer. Gao *et al.* [175] have shown that Fe$_3$O$_4$-CdSe NPs exhibit quantum yield as high as 38 per cent. Such fluorescence enables the intracellular detection of the NPs; however, no results were reported regarding their magnetic properties nor their relaxivity. In order to favour metallic materials, which exhibit higher magnetization, a solution consists in incorporating preformed magnetic NPs and QDs into an isolating matrix (such as silica) [176]. However, the resulting object exhibits a high hydrodynamic volume, which may be a drawback for further

in vivo applications and prevents the diffusion of water proton in the vicinity of the magnetic NPs, resulting in poor relaxivity [177]. Deka *et al.* [178] have reported a promising approach based on the intercalation of a semiconductor with a larger band gap between the metallic part and the QD, which may result in decoupling QD and metal electronic states. CdSe@CdS decorated with Co tips exhibited preserved magnetic properties (M_S = 148 emu/g$_{Co}$) but partially quenched fluorescence (QY = 3%). Optimization of the spacer nature and thickness could be pursued to retain both physical properties unaltered.

7. Conclusion

In this review paper, we have presented the potentiality of a new generation of optimized contrast agents, based on metallic NPs and Hg, Cd, Pb, As free QDs, for, respectively, MRI and NIR imaging. Though extensive literature can be found on well-established iron oxide NPs or Cd-based QDs, only a few reports outline the requirements that the new probe generation should fulfil. Thanks to the description of the physics of the imaging techniques, optimized materials could be illuminated for as long as the syntheses appropriate to the corresponding NPs. Surface engineering strategies to ensure the biodistribution and the specific targeting of inorganic NPs were reviewed. The resulting NPs combine, through a complex architecture: the optimized inorganic core surrounded by a non-porous coating shell, to ensure the stability of the core, an organic corona to reach adequate biodistribution and targeting moities to enhance the specific cellular uptake. Few results demonstrate the *in vivo* potentiality of these new generations of probes. Drastic enhancement of relaxivity (up to 10^5 times) was observed for Co-based NPs, while impressive fluorescent results were obtained for Cd-free InP/ZnS QDs. The next step towards the optimization of contrast agents relies on the integration, within a single object, of MRI and NIR imaging potentialities. Such multi-modal NPs, though extremely promising, require the strict decoupling of semiconducting and metallic electronic states. The introduction of a large gap semiconductor spacer could be the most promising approach which could yield unaltered magnetic and optic properties.

References

1. Cassidy PJ, Radda GK. 2005 Molecular imaging perspectives. *J. R. Soc. Interface* **2**, 133–144. (doi:10.1098/rsif.2005.0040)

2. Cho EC, Glauss C, Chen J, Welch MJ, Xia Y. 2010 Inorganic nanoparticle-based contrast agents for moleuclar imaging. *Trends Mol. Med.* **16**, 561–573. (doi:10.1016/j.molmed.2010.09.004)

3. Lee D-E, Koo H, Sun I-C, Ryu JH, Kim K, Kwon IC. 2012 Multifunctional nanoparticles for multimodal imaging and theragnosis. *Chem. Soc. Rev.* **41**, 2656–2672. (doi:10.1039/c2cs15261d)

4. Hötzer B, Medintz IL, Hildebrandt N. 2012 Fluorescence in nanobiotechnology: sophisticated fluorophores for novel applications. *Small* **8**, 2297–2326. (doi:10.1002/smll.201200109)

5. Lacroix L-M, Ho D, Sun S. 2010 Recent advances in magnetic nanoparticles for diagnostic and therapeutic applications. *Curr. Top. Med. Chem.* **10**, 1184–1197.

6. Finney EE, Finke RG. 2008 Nanocluster nucleation and growth kinetic and mechanistic studies: a review emphasizing transitionmetal nanoclusters. *J. Colloid Interface Sci.* **317**, 351–374. (doi:10.1016/j.jcis.2007.05.092)

7. LaMer VK, Dinegra RH. 1950 Theory, production and mechanism of formation of monodispersed hydrosols. *J. Am. Chem. Soc.* **72**, 4847–4854. (doi:10.1021/ja01167a001)

8. Park J, Joo J, Kwon SG, Jang Y, Hyeon T. 2007 Synthesis of monodisperse spherical nanocrystals. *Angew. Chem. Int. Ed.* **46**, 4630–4660. (doi:10.1002/anie.200603148)

9. Shevchenko EV, Talapin DT, Schnablegger H, Kornowski A, Festin O, Svedlinh P, Haase M, Weller H. 2002 Study of nucleation and growth in the organometallic synthesis of magnetic alloy nanocrystals: the role of nucleation rate in size control of CoPt$_3$ nanocrystals. *J. Am. Chem. Soc.* **125**, 9090–9101. (doi:10.1021/ja029937l)

10. Lin W, Hyeon T, Lanza GM, Zhang M, Maede TJ. 2009 Magnetic nanoparticles for early detection of cancer by magnetic resonance imaging. *MRS Bull.* **34**, 441–448. (doi:10.1557/mrs2009.120)

11. Caravan P, Ellison JL, McMurry TJ, Lauffer RB. 1999 Gadolinium(III) chelates as MRI contrast agents:

structure, dynamics and applications. *Chem. Rev.* **99**, 2293–2352. (doi:10.1021/cr980440x)

12. Caravan P. 2006 Strategies for increasing the sensitivity of gadolinium based MRI contrast agents. *Chem. Soc. Rev.* **35**, 512–523. (doi:10.1039/B510982P)

13. De Leon-Rodriguez LM, Lubag AJM, Malloy CR, Martinez GV, Gillies RJ, Sherry AD. 2011 Responsive MRI agents for sensing metabolism *in vivo*. *Acc. Chem. Res.* **42**, 948–957. (doi:10.1021/ar800237f)

14. Na HB, Song IC, Hyeon T. 2009 Inorganic nanoparticles for MRI contrast agents. *Adv. Mater.* **21**, 2133–2148. (doi:10.1002/adma.200802366)

15. Cheon J, Lee J-H. 2008 Synergistically integrated nanoparticles as multimodal probes for nanobiotechnology. *Acc. Chem. Res.* **41**, 1630–1640. (doi:10.1021/ar800054c)

16. Lee J-H *et al.* 2007 Artificially engineered magnetic nanoparticles for ultra-sensitive molecular imaging. *Nat. Med.* **13**, 95–99. (doi:10.1038/nm1467)

17. Duan H, Kuang M, Wang X, Wang YA, Mao H, Nie S. 2008 Reexamining the effects of particle size and surface chemistry on the magnetic properties of iron oxide nanocrystals: new insights into spin disorder and proton relaxivity. *J. Phys. Chem. C* **112**, 8127–8131. (doi:10.1021/jp8029083)

18. Hadjipanayis CG, Bonder MJ, Balakrishnan S, Wang X, Mao H, Hadjipanayis GC. 2008 Metallic iron nanoparticles for MRI contrast enhancement and local hyperthermia. *Small* **4**, 1925–1929. (doi:10.1002/smll.200800261)

19. Cheong S *et al.* 2011 Simple synthesis and functionalization of iron nanoparticles for magnetic resonance imaging. *Angew. Chem. Int. Ed.* **50**, 4206–4209. (doi:10.1002/anie.201100562)

20. Lacroix L-M, Huls NF, Ho D, Sun X, Cheng K, Sun S. 2011 Stable single-crystalline body centered cubic Fe nanoparticles. *Nano Lett.* **11**, 1641–1645. (doi:10.1021/nl200110t)

21. Bouchard L-S, Anwar MS, Liu GL, Hann B, Xie ZH, Gray JW, Wang X, Pines A, Chen FF. 2009 Picomolar sensitivity MRI and photoacoustic imaging of cobalt nanoparticles. *Proc. Nat Acad. Soc. USA* **106**, 4085–4089. (doi:10.1073/pnas.0813019106)

22. Seo WS *et al.* 2006 FeCo/graphitic-shell nanocrystals as advanced magnetic-resonance-imaging and near-infrared agents. *Nat. Mater.* **5**, 971–976. (doi:10.1038/nmat1775)

23. Maesono S, Suzuki T, Saita S. 2008 Superparamagnetic FePt nanoparticles as excellent MRI contrast agents. *J. Magn. Magn. Mater.* **320**, L79–L83. (doi:10.1016/j.jmmm.2008.01.026)

24. Tromsdorf UI *et al.* 2007 Size and surface effects on the MRI relaxivity of manganese ferrite nanoparticle contrast agents. *Nano Lett.* **7**, 2422–2427. (doi:10.1021/nl071099b)

25. Lee N, Choi Y, Lee Y, Park M, Moon WK, Choi SH, Hyeon T. 2012 Water-dispersible ferromagnetic iron oxide nanocubes with extremely high r_2 relaxivity for highly sensitive *in vivo* MRI of tumors. *Nano Lett.* **12**, 3127–3131. (doi:10.1021/nl3010308)

26. Lee JS, Tan RP, Wu JH, Kim YK. 2011 Effect of interparticle interactions and size dispersión in

magnetic nanoparticle assemblies: a static and dynamic study. *Appl. Phys. Lett.* **99**, 062506. (doi:10.1063/1.3624833)

27. Yang Y, Liu X-L, Yi J-B, Yang Y, Fan H-M, Ding J. 2012 Stable vortex magnetite nanorings colloid: micromagnetic simulation and experimental demonstration. *J. Appl. Phys.* **111**, 044303. (doi:10.1063/1.3684963)

28. Snoeck E, Gatel C, Lacroix L-M, Blon T, Lachaize S, Carrey J, Respaud M, Chaudret B. 2008 Magnetic configurations of 30 nm iron nanocubes studied by electron holography. *Nano Lett.* **8**, 4293–4298. (doi:10.1021/nl801998x)

29. Lacroix L-M, Lachaize S, Hue F, Gatel C, Blon T, Tan RP, Carrey J, Warot-Fonrose B, Chaudret B. 2012 Stabilization vortices in interacting nano-objects: a chemical approach. *Nano Lett.* **12**, 3245–3250. (doi:10.1021/nl3012616)

30. Yang F, Jin C, Subedi S, Lee CL, Wang Q, Jiang Y, Li J, Di Y, Fu D. 2012 Emerging inorganic nanomaterials for pancreatic cancer diagnosis and treatment. *Cancer Treat. Rev.* **38**, 566–579. (doi:10.1016/j.ctrv.2012.02.003)

31. Huang S-H, Juang R-S. 2011 Biochemical and biomedical applications of multifunctional magnetic nanoparticles: a review. *J. Nanopart. Res.* **13**, 4411–4430. (doi:10.1007/s11051-011-0551-4)

32. Huang S, Yan W, Hu G, Wang L. 2012 Facile and green synthesis of biocompatible and bioconjugatable magnetite nanofluids for high-resolution T_2 MRI contrast agents. *J. Phys. Chem. C* **116**, 20 558–20 563. (doi:10.1021/jp305211d)

33. Laurent S, Forge D, Port M, Roch A, Robic C, Vander Elst L, Muller RN. 2008 Magnetic iron oxide nanoparticles: synthesis, stabilization, vectorization, physicochemical characterizations, and biological applications. *Chem. Rev.* **108**, 2064–2110. (doi:10.1021/cr068445e)

34. Park J *et al.* 2005 One-nanometer-scale size-controlled synthesis of monodisperse magnetic iron oxide nanoparticles. *Angew. Chem. Int. Ed.* **44**, 2872–2877. (doi:10.1002/anie.200461665)

35. Sun S, Zeng H. 2002 Size-controlled synthesis of magnetite nanoparticles. *J. Am. Chem. Soc.* **124**, 8204–8205. (doi:10.1021/ja026501x)

36. Reddy LH, Arias JL, Nicolas J, Couvreur P. 2012 Magnetic nanoparticles: design and characterization, toxicity and biocompatibility, pharmaceutical and biomedical applications. *Chem. Rev.* **112**, 5818–5878. (doi:10.1021/cr300068p)

37. Lee N, Hyeon T. 2012 Designed synthesis of uniformly sized iron oxide nanoparticles for efficient magnetic resonance imaging contrast agents. *Chem. Soc. Rev.* **41**, 2575–2589. (doi:10.1039/C1CS15248C)

38. Sun S, Zeng H, Robinson DB, Raoux S, Rice PM, Wang SX, Li G. 2004 Monodisperse MFe_2O_4 (M= Fe, Co, Mn) nanoparticles. *J. Am. Chem. Soc.* **126**, 273–279. (doi:10.1021/ja0380852)

39. Farrell D, Majetich SA, Wilcoxon JP. 2003 Preparation and characterization of monodisperse Fe nanoparticles. *J. Phys. Chem. B* **107**, 11 022–11 030. (doi:10.1021/jp0351831)

40. Pei W, Kakibe S, Ohta I, Takahashi M. 2005 Controlled monodisperse Fe nanoparticles synthesized by chemical method. *IEEE Trans. Magn.* **41**, 3391–3393. (doi:10.1109/TMAG.2005.855207)

41. Shavel A, Rodriguez-Gonzalez B, Spasova M, Farle M, Liz-Marzan LM. 2007 Synthesis and characterization of iron/iron oxide core/shell nanocubes. *Adv. Funct. Mater.* **17**, 3870–3876. (doi:10.1002/adfm.200700494)

42. Lacroix L-M, Lachaize S, Falqui A, Respaud M, Chaudret B. 2009 Iron nanoparticle growth in organic superstructures. *J. Am. Chem. Soc.* **131**, 549–557. (doi:10.1021/ja805719c)

43. Guo Z, Henry LL, Palshin V, Podlaha EJ. 2006 Synthesis of poly(methyl methacrylate) stabilized colloidal zero-valence metallic nanoparticles. *J. Mater. Chem.* **16**, 1772–1777. (doi:10.1039/b515565g)

44. Puntes VF, Krishnan KM, Alivisatos AP. 2001 Colloidal nanocrystal shape and size control: the case of cobalto. *Science* **291**, 2115–2117. (doi:10.1126/science.1057553)

45. Sun S, Murray CB. 1999 Synthesis of monodisperse cobalt nanocrystals and their assembly into magnetic superlattices. *J. Appl. Phys.* **85**, 4325–4330. (doi:10.1063/1.370357)

46. Soumare Y, Garcia C, Maurer T, Chaboussant G, Ott F, Fiévet F, Piquemal J-Y, Viau G. 2009 Kinetically controlled synthesis of hexagonally close-packed cobalt nanorods with high magnetic coercivity. *Adv. Funct. Mater.* **19**, 1971–1977. (doi:10/1002/adfm.200800822)

47. Liakakos N *et al.* 2012 The big impact of a small detail: cobalt nanocrystal polymorphism as a result of precursor addition rate during stock solution preparation. *J. Am. Chem. Soc.* **134**, 17 922–17 931. (doi:10.1021/ja304487b)

48. Dumestre F, Chaudret B, Amiens C, Respaud M, Fejes P, Renaud P, Zurcher P. 2003 Unprecedented crystalline super-lattices of monodisperse cobalt nanorods. *Angew. Chem. Int. Ed.* **42**, 5213–5216. (doi:10.1002/anie.200352090)

49. Ogawa T, Takano H, Kura H, Takahashi M. 2012 Synthesis of Fe-Co nanoparticles with high saturation magnetization by low temperature post-annealing. *J. Appl. Phys.* **111**, 07B533. (doi:10.1063/1.3679027)

50. Wang C, Peng S, Lacroix L-M, Sun S. 2009 Synthesis of high magnetic moment CoFe nanoparticles via interfacial diffusion in core/shell structured Co/Fe nanoparticles. *Nano Res.* **2**, 380–385. (doi:10.1007/s12274-009-9037-4)

51. Desvaux C, Amiens C, Fejes P, Renaud P, Respaud M, Lecante P, Snoeck E, Chaudret B. 2005 Multimillimetre-large superlattices of air-stable iron-cobalt nanoparticles. *Nat. Mater.* **4**, 750–753. (doi:10.1038/nmat1480)

52. Chaubey GS, Barcena C, Poudyal N, Rong C, Gao J, Sun S, Liu JP. 2007 Synthesis and stabilization of FeCo Nanoparticles. *J. Am. Chem. Soc.* **129**, 7214–7215. (doi:10.1021/ja0708969)

53. Sun S, Murray CB, Weller D, Folks L, Moser A. 2000 Monodisperse FePt nanoparticles and ferromagnetic

FePt nanocrystal superlattices. *Science* **287**, 1989–1992. (doi:10.1126/science.287.5460.1989)

54. Elkins KE, Chaubey GS, Nandwana V, Liu JP. 2008 A novel approach to synthesis of FePt magnetic nanoparticles. *J. Nano. Res.* **1**, 23–30. (doi:10.4028/www.scientific.net/JNanoR.1.23)

55. Sun S, Anders S, Thomson T, Baglin JEE, Toney MF, Hamann HF, Murray CB, Terris BD. 2003 Controlled synthesis and assembly of FePt nanoparticles. *J. Phys. Chem. B* **107**, 5419–5425. (doi:10.1021/jp027314o)

56. Huber D. 2005 Synthesis, properties, and applications of iron nanoparticles. *Small* **1**, 482–501. (doi:10.1002/smll.200500006)

57. Yang H, Ito F, Hasegawa D, Ogawa T, Takahashi M. 2007 Facile large-scale synthesis of monodisperse Fe nanoparticles by modest-temperature decomposition of iron carbonyl. *J. Appl. Phys.* **101**, 09J112. (doi:10.1063/1.2711391)

58. Meffre A, Mehdaoui B, Kelsen V, Fazzini PF, Carrey J, Lachaize S, Respaud M, Chaudret B. 2012 A simple chemical route toward monodisperse iron carbide nanoparticles displaying tunable magnetic and unprecedented hyperthermia properties. *Nano Lett.* **12**, 4722–4728. (doi:10.1021/nl302160d)

59. Dumestre F, Chaudret B, Amiens C, Renaud P, Fejes P. 2004 Superlattices of iron nanocubes synthesized from Fe[N(SiMe$_3$)$_2$]$_2$. *Science* **303**, 821–823. (doi:10.1126/science.1092641)

60. Meffre A, Lachaize S, Gatel C, Respaud M, Chaudret B. 2011 Use of long chain amine as a reducing agent for the synthesis of high quality monodisperse iron(0) nanoparticles. *J. Mater. Chem.* **21**, 13 464–13 469. (doi:10.1039/C1JM12127H)

61. Lacroix L-M, Lachaize S, Carrey J, Respaud M, Chaudret B. 2011 Iron nanoparticles with tuneable sizes for hyperthermia applications. *L'Act. Chim.* **351**, 28–35.

62. Keng PY, Shim I, Korth BD, Douglas JF, Pyun J. 2009 Synthesis and self assembly of polymer-coated ferromagnetic nanoparticles. *ACS Nano* **1**, 279–292. (doi:10.1021/nn7001213)

63. Osuna J, de Caro D, Amiens C, Chaudret B, Snoeck E, Respaud M, Broto J-M, Fert A. 1996 Synthesis, characterization, and magnetic properties of cobalt nanoparticles from an organometallic precursor. *J. Phys. Chem.* **100**, 14 571–14 574. (doi:10.1021/jp961086e)

64. Sun S. 2006 Recent advances in chemical synthesis, self-assembly, and applications of FePt nanoparticles. *Adv. Mater.* **18**, 393–403. (doi:10.1002/adma.200501464)

65. Gao J *et al.* 2008 Multifunctional yolk-shell nanoparticles: a potential MRI contrast and anticancer agent. *J. Am. Chem. Soc.* **130**, 11 828–11 833. (doi:10.1021/ja803920b)

66. Pansare VJ, Hejazi S, Faenza WJ, Prud'homme RK. 2012 Review of long-wavelength optical and nir imaging materials: contrast agents, fluorophores, and multifunctional nano carriers. *Chem. Mater.* **24**, 812–827. (doi:10.1021/cm2028367)

67. Weissleder R. 2001 A clearer vision for *in vivo* imaging. *Nat. Biotechnol.* **19**, 316–317. (doi:10.1038/86684)

68. Frangioni JV. 2003 *In vivo* near-infrared fluorescence imaging. *Curr. Opin. Chem. Biol.* **7**, 626–634. (doi:10.1016/j.cbpa.2003.08.007)

69. Resch-Genger U, Grabollel M, Cavaliere-Jaricot S, Nitschke R, Nann T. 2008 Quantum dots versus organic dyes as fluorescent labels. *Nat. Methods* **5**, 763–775. (doi:10.1038/nmeth.1248)

70. Berlier JE *et al.* 2003 Quantitative comparison of long-wavelength alexa fluor dyes to Cy dyes: fluorescence of the dyes and their bioconjugates. *J. Histochem. Cytochem.* **51**, 1699–1712. (doi:10.1177/002215540305101214)

71. Aswathy RG, Yoshida Y, Maekawa T, Kumar DS. 2010 Near-infrared quantum dots for deep tissue imaging. *Anal. Bioanal. Chem.* **397**, 1417–1435. (doi:10.1007/s00216-010-3643-6).

72. Shan J, Uddi M, Wei R, Yao N, Ju Y. 2010 The Hidden effects of particle shape and criteria for evaluating the upconversion luminescence of the lanthanide doped nanophosphors. *J. Phys. Chem. C* **114**, 2452–2461. (doi:10.1021/jp908976n).

73. Chatterjee DK, Gnanasammandhan MK, Zhang Y. 2010 Small upconverting fluorescent nanoparticles for biomedical applications. *Small* **6**, 2781–2795. (doi:10.1002/smll.201000418)

74. Luo Z, Yuan X, Yu Y, Zhang Q, Leong DT, Lee JY, Xie J. 2012 From aggregation-induced emission of Au(I)–thiolate complexes to ultrabright Au(0)@Au(I)–thiolate core–shell nanoclusters. *J. Am. Chem. Soc.* **134**, 16 662–16 670. (doi:10.1021/ja306199p).

75. Baba K, Nishida K. 2012 Single-molecule tracking in living cells using single quantum dot applications. *Theranostics* **2**, 655–667. (doi:10.7150/thno.3890)

76. Alivisatos AP. 1996 Perspectives on the physical chemistry of semiconductor nanocrystals. *J. Phys. Chem.* **100**, 13 226–13 239. (doi:10.1021/jp9535506)

77. Smith AM, Nie S. 2010 Semiconductor nanocrystals: structure, properties, and band gap engineering. *Acc. Chem. Res.* **43**, 190–200. (doi:10.1021/ar9001069)

78. de Mello Donega C. 2011 Synthesis and properties of colloidal heteronanocrystals. *Chem. Soc. Rev.* **40**, 1512–1546. (doi:10.1039/c0cs00055h)

79. Bailey RE, Nie S. 2003 Alloyed semiconductor quantum dots: tuning the optical properties without changing the particle size. *J. Am. Chem. Soc.* **125**, 7100–7106. (doi:10.1021/ja035000o)

80. Gaponik N, Rogach AL. 2008 Aqueous synthesis of semiconductor nanocrystals. In *semiconductor nanocrystals quantum dots* (ed. AL Rogach), pp. 73–100. New York, NY: Springer.

81. Xue B, Deng D-W, Cao J, Liu F, Li X, Akers W, Achilefu S, Gu Y-Q. 2012 Synthesis of NAC capped near infrared-emitting CdTeS alloyed quantum dots and application for *in vivo* early tumor imaging. *Dalton Trans.* **41**, 4935–4947. (doi:10.1039/c2dt12436j)

82. Pons T, Lequeux N, Mahler B, Sasnouski S, Fragola A, Dubertret B. 2009 Synthesis of near-infrared-emitting, water-soluble CdTeSe/CdZnS core/shell quantum dots. *Chem. Mater.* **21**, 1418–1424. (doi:10.1021/cm8027127)

83. Harrison MT, Kershaw SV, Burt MG, Eychmuller A, Weller H, Rogach AL. 2000 Wet chemical synthesis and spectroscopic study of CdHgTe nanocrystals with strong near-infrared luminescence. *Mater. Sci. Eng.* **B69–70**, 355–360. (doi:10.1016/S0921-5107(99)00254-8)

84. Kovalenko MV, Kaufmann E, Pachinger D, Roither J, Huber M, Stangl J, Hesser G, Schaffler F, Heiss W. 2006 Colloidal HgTe nanocrystals with widely tunable narrow band gap energies: from telecommunications to molecular vibrations. *J. Am. Chem. Soc.* **128**, 3516–3517. (doi:10.1021/ja058440j)

85. Cademartiri L, Montanari E, Calestani G, Migliori A, Guagliardi A, Ozin GA. 2006 Size-dependent extinction coefficients of PbS quantum dots. *J. Am. Chem. Soc.* **128**, 10 337–10 346. (doi:10.1021/ja063166u).

86. Hines MA, Scholes GD. 2003 Colloidal PbS nanocrystals with size-tunable near-infrared emission: observation of post-synthesis self-narrowing of the particle size distribution. *Adv. Mater.* **15**, 1844–1849. (doi:10.1002/adma.200305395)

87. Akhtar J *et al.* 2011 Controlled synthesis of tuned bandgap nanodimensional alloys of PbS$_x$Se$_{1-x}$. *J. Am. Chem. Soc.* **133**, 5602–5609. (doi:10.1021/ja200750s)

88. Moreels I, Lambert K, De Muynck D, Vanhaecke F, Poelman D, Martins JC, Allan G, Hens Z. 2007 Composition and size-dependent extinction coefficient of colloidal PbSe quantum dots. *Chem. Mater.* **19**, 6101–6106. (doi:10.1021/cm071410q)

89. Murphy JE, Beard MC, Norman AG, Ahrenkiel SP, Johnson JC, Yu P, Micic OI, Ellingson RJ, Nozik AJ. 2006 PbTe colloidal nanocrystals: synthesis, characterization, and multiple exciton generation. *J. Am. Chem. Soc.* **128**, 3241–3247. (doi:10.1021/ja0574973)

90. Xie R, Battaglia D, Peng X. 2007 Colloidal InP nanocrystals as efficient emitters covering blue to near-infrared. *J. Am. Chem. Soc.* **128**, 15 432–15 433. (doi:10.1021/ja076363h)

91. Xie R, Peng X. 2009 Synthesis of Cu-doped InP Nanocrystals (d-dots) with ZnSe diffusion barrier as efficient and color-tunable NIR emitters. *J. Am. Chem. Soc.* **131**, 10 645–10 651. (doi:10.1021/ja903558r)

92. Kim S-W, Zimmer JP, Ohnishi S, Tracy JB, Frangioni JV, Bawendi MG. 2005 Engineering InAs$_x$P$_{1-x}$/InP/ZnSe III-V alloyed core/shell quantum dots for the near-infrared. *J. Am. Chem. Soc.* **127**, 10 526–10 532. (doi:10.1021/ja0434331)

93. Xie R, Peng X. 2008 Synthetic scheme for high-quality InAs nanocrystals based on self-focusing and one-pot synthesis of InAs-based core–shell nanocrystals. *Angew. Chem. Int. Ed.* **47**, 7677–7680. (doi:10.1002/anie.200802867)

94. Xie R, Zhang J, Zhao F, Yang W, Peng X. 2010 Synthesis of monodisperse, highly emissive, and size-tunable Cd$_3$P$_2$ nanocrystals. *Chem. Mater.* **22**, 3820–3822. (doi:10.1021/cm1008653)

95. Harris DK, Allen PM, Han H-S, Walker BJ, Lee J, Bawendi MG. 2011 Synthesis of cadmium arsenide

quantum dots luminescent in the infrared. *J. Am. Chem. Soc.* **133**, 4676–4679. (doi:10.1021/ja1101932)

96. Xie R, Rutherford M, Peng X. 2009 Formation of high-quality I-III-VI semiconductor nanocrystals by tuning relative reactivity of cationic precursors. *J. Am. Chem. Soc.* **131**, 5691–5697. (doi:10.1021/ja9005767)

97. Cassette E, Pons T, Bouet C, Helle M, Bezdetnaya L, Marchal F, Dubertret B. 2010 Synthesis and characterization of near-infrared Cu-In-Se/ZnS core/shell quantum dots for *in vivo* imaging. *Chem. Mater.* **22**, 6117–6124. (doi:10.1021/cm101881b)

98. Ruddy DA, Johnson JC, Smith ER, Neale NR. 2010 Size and bandgap control in the solution-phase synthesis of near-infrared-emitting germanium nanocrystals. *ACS Nano* **4**, 7459–7466. (doi:10.1021/nn102728u)

99. Lee DC, Pietryga JM, Robel I, Werder DJ, Schaller RD, Klimov VI. 2009 Colloidal synthesis of infrared-emitting germanium nanocrystals. *J. Am. Chem. Soc.* **131**, 3436–3437. (doi:10.1021/ja809218s)

100. Jiang P, Zhu C-N, Zhang Z-L, Tian Z-Q, Pang D-W. 2012 Water-soluble Ag$_2$S quantum dots for near-infrared fluorescence imaging *in vivo*. *Biomaterials* **33**, 5130–5135. (doi:10.1016/j.biomaterials.2012.03.059)

101. Yarema M *et al*. 2011 Infrared emitting and photoconducting colloidal silver chalcogenide nanocrystal quantum dots from a silylamide-promoted synthesis. *ACS Nano* **5**, 3758–3765. (doi:10.1021/nn2001118)

102. Reiss P, Protière M, Li L. 2009 Core/Shell semiconductor nanocrystals. *Small* **5**, 154–168. (doi:10.1002/smll.200800841)

103. Gaponik N, Hickey SG, Dorfs D, Rogach AL, Eychmüller A. 2010 Progress in the light emission of colloidal semiconductor nanocrystals. *Small* **6**, 1364–1378. (doi:10.1002/smll.200902006)

104. Wang C, Gao X, Su X. 2010 *In vitro* and *in vivo* imaging with quantum dots. *Anal. Bioanal. Chem.* **397**, 1397–1415. (doi:10.1007/s00216-010-3481-6)

105. Murray CB, Norris DJ, Bawendi MG. 1993 Synthesis and characterization of nearly monodisperse CdE (E=S, Se, Te) semiconductor nanocrystallites. *J. Am. Chem. Soc.* **115**, 8706–8715. (doi:10.1021/ja00072a025)

106. Peng ZA, Peng X. 2001 Formation of high-quality CdTe, CdSe, and CdS nanocrystals using CdO as precursor. *J. Am. Chem. Soc.* **123**, 183–184. (doi:10.1021/ja003633m)

107. Yu W, Peng X. 2002 Formation of high-quality CdS and Other II–VI semiconductor nanocrystals in noncoordinating solvents: tunable reactivity of monomers. *Angew. Chem. Int. Ed.* **41**, 2368–2371. (doi:10.1002/1521-3773)

108. Siy JT, Brauser EM, Bartl MH. 2011 Low-temperature synthesis of CdSe nanocrystal quantum dots. *Chem. Commun.* **47**, 364–366. (doi:10.1039/c0cc02304c)

109. Murray CB, Sun SH, Gaschler W, Doyle H, Betley TA, Kagan CR. 2001 Colloidal synthesis of nanocrystals and nanocrystal superlattices. *IBM J. Res. Dev.* **45**, 47–56. (doi:10.1147/rd.451.0047)

110. Lu WG, Fang JY, Stokes KL, Lin J. 2004 Shape evolution and self assembly of monodisperse PbTe nanocrystals. *J. Am. Chem. Soc.* **126**, 11 798–11 799. (doi:10.1021/ja0469131)

111. Rogach AL, Eychmüller A, Hickey SG, Kershaw SV. 2007 Infrared-emitting colloidal nanocrystals: synthesis, assembly, spectroscopy, and applications. *Small* **3**, 536–557. (doi:10.1002/smll.200600625)

112. Ojo W-S, Xu S, Delpech F, Nayral C, Chaudret B. 2012 Room-temperature synthesis of air-stable and size-tunable luminescent ZnS-coated Cd$_3$P$_2$ nanocrystals with high quantum yields. *Angew. Chem. Int. Ed.* **51**, 738–741. (doi:10.1002/anie.201104864)

113. Bottrill M, Green M. 2011 Some aspects of quantum dot toxicity. *Chem. Commun.* **47**, 7039–7050. (doi:10.1039/c1cc10692a)

114. Antunez PD, Buckley JJ, Brutchey RL. 2011 Tin and germanium monochalcogenide IV–VI semiconductor nanocrystals for use in solar cells. *Nanoscale* **3**, 2399–2411. (doi:10.1039/C1NR10084J)

115. Kovalenko MV, Heiss W, Shevchenko EV, Lee J-S, Schwinghammer H, Alivisatos AP, Talapin DV. 2007 SnTe nanocrystals: a new example of narrow-gap semiconductor quantum dots. *J. Am. Chem. Soc.* **129**, 11 354–11 355. (doi:10.1021/ja074481z)

116. Micic OI, Curtis CJ, Jones KM, Sprague JR, Nozik AJ. 1994 Synthesis and characterization of InP quantum dots. *J. Phys. Chem.* **98**, 4966–4969. (doi:10.1021/j100070a004)

117. Battaglia D, Peng X. 2002 Formation of high quality InP and InAs nanocrystals in a noncoordinating solvent. *Nano Lett.* **2**, 1027–1030. (doi:10.1021/nl025687v)

118. Cros-Gagneux A, Delpech F, Nayral C, Cornejo A, Coppel Y, Chaudret B. 2010 Surface chemistry of InP quantum dots: a comprehensive study. *J. Am. Chem. Soc.* **132**, 18 147–18 157. (doi:10.1021/ja104673y)

119. Guzelian AA, Banin U, Kadavanich AV, Peng X, Alivisatos AP. 1996 Colloidal chemical synthesis and characterization of InAs nanocrystal quantum dots. *Appl. Phys. Lett.* **69**, 1432–1434. (doi:10.1063/1.117605)

120. Choi HS, Ipe BI, Misra P, Lee JH, Bawendi MG, Frangioni JV. 2009 Tissue- and organ-selective biodistribution of NIR fluorescent quantum dots. *Nano Lett.* **9**, 2354–2359. (doi:10.1021/nl900872r)

121. Malik MA, O'Brien P, Revaprasadu N. 1999 A novel route for the preparation of CuSe and CuInSe2 nanoparticles. *Adv. Mater.* **11**, 1441–1444. (doi:10.1002/(SICI)1521-4095(199912))

122. Castro SL, Bailey SG, Raffaelle RP, Banger KK, Hepp AF. 2003 Nanocrystalline chalcopyrite materials (CuInS$_2$ and CuInSe$_2$) via low-temperature pyrolysis of molecular single-source precursors. *Chem. Mater.* **15**, 3142–3147. (doi:10.1021/cm034161o)

123. Zhong H, Li Y, Ye M, Zhu Z, Zhou Y, Yang C, Li Y. 2007 A facile route to synthesize chalcopyrite CuInSe$_2$ nanocrystals in non-coordinating Solvent. *Nanotechnology* **18**, 025602. (doi:10.1088/0957-4484/18/2/025602)

124. Lambert TN, Andrews NL, Gerung H, Boyle TJ, Oliver JM, Wilson BS, Han SM. 2007 Water-soluble germanium(0) nanocrystals: cell recognition and near-infrared photothermal conversion properties. *Small* **3**, 691–699. (doi:10.1002/smll.200600529)

125. Du Y, Xu B, Fu T, Cai M, Li F, Zhang Y, Wang Q. 2010 Near-infrared photoluminescent Ag$_2$S quantum dots from a single source precursor. *J. Am. Chem. Soc.* **132**, 1470–1471. (doi:10.1021/ja909490r)

126. Gu Y-P, Cui R, Zhang Z-L, Xie Z-X, Pang D-W. 2012 Ultrasmall near-infrared Ag$_2$Se quantum dots with tunable fluorescence for *in vivo* imaging. *J. Am. Chem. Soc.* **134**, 79–82. (doi:10.1021/ja2089553)

127. Hocaoglu I, Cizmeciyan MN, Erdem R, Ozen C, Kurt A, Sennaroagluad A, Acar HY. 2012 Development of highly luminescent and cytocompatible near-IR-emitting aqueous Ag$_2$S quantum dots. *J. Mater. Chem.* **22**, 14 674–14 681. (doi:10.1039/c2jm31959d)

128. Tian Z-Q, Zhu C-N, Zhang Z-L. 2012 Emission-tunable near-infrared Ag$_2$S quantum dots. *Chem. Mater.* **24**, 3–5. (doi:10.1021/cm202543m)

129. Peng S, Wang C, Xie J, Sun S. 2006 Synthesis and stabilization of monodisperse Fe nanoparticles. *J. Am. Chem. Soc.* **128**, 10 676–10 677. (doi:10.1021/ja063969h)

130. Gao J, Liang G, Zhang B, Kuang Y, Zhang X, Xu B. 2007 FePt@CoS2 yolk-shell nanocrystals as a potent agent to kill HeLa cells. *J. Am. Chem. Soc.* **129**, 1428–1433. (doi:10.1021/ja067785e)

131. Shubayev VI, Pisanic II TR, Jin S. 2009 Magnetic nanoparticles for theragnostics. *Adv. Drug. Deliv. Rev.* **61**, 467–477. (doi:10.1016/j.addr.2009.03.007)

132. Dreaden EC, Alkilany AM, Huang X, Murphy CJ, El-Sayed MA. 2012 The golden age: gold nanoparticles for biomedicine. *Chem. Soc. Rev.* **41**, 2740–2779. (doi:10.1039/c1cs15237h)

133. Lee W-R, Kim MG, Choi J-R, Park J-I, Ko SJ, Oh SJ, Cheon J. 2005 Redox transmetalation process as a generalized synthetic strategy for core shell magnetic nanoparticles. *J. Am. Chem. Soc.* **127**, 16 090–16 097. (doi:10.1021/ja053659j)

134. Chaudhuri RG, Paria S. 2012 Core/shell nanoparticles: classes, properties, synthesis mechanisms, characterization, and applications. *Chem. Rev.* **112**, 2373–2433. (doi:10.1021/cr100449n)

135. Wetz F, Soulantica K, Falqui A, Respaud M, Snoeck E, Chaudret B. 2007 Hybrid Co-Au nanorods: controlling Au nucleation and location. *Angew. Chem. Int. Ed.* **46**, 7079–7081. (doi:10.1002/anie.200702017)

136. Schrand AM, Rahman MF, Hussain SM, Schlager JJ, Smith DA, Syed AF. 2010 Metal-based nanoparticles and their toxicity assessment. *WIREs Nanomed. Nanobiotech.* **2**, 544–568. (doi:10.1002/wnan.103)

137. Guerrero-Martinez A, Perez-Juste J, Liz-Marzan LM. 2010 Recent progress on silica coating of nanoparticles and related nanomaterials. *Adv. Mater.* **22**, 1182–1195. (doi:10.1002/adma.200901263)

138. El Hawi N, Nayral C, Delpech F, Coppel Y, Cornejo A, Castel A, Chaudret B. 2009 Silica nanoparticles Brown and stabilized in organic nonalcoholic media. *Langmuir* **25**, 7540–7546. (doi:10.1021/la9011789)

139. Delpech F, Nayral C, El Hawi N. 2008 *Manufacturing process for silica-coated metal nanoparticles.* International Patent PCT, Patent no. WO 2009071794 (filing date: 18 November 2008).

140. Ivanov SA, Piryatinski A, Nanda J, Tretiak S, Zavadil KR, Wallace WO, Werder D, Klimov VI. 2007 Type-II core/shell CdS/ZnSe nanocrystals: synthesis, electronic structures, and spectroscopic properties. *J. Am. Chem. Soc.* **129**, 11 708–11 719. (doi:10.1021/ja068351m)

141. Li L, Protière M, Reiss P. 2008 Economic synthesis of high quality InP nanocrystals using calcium phosphide as the phosphorus precursor. *Chem. Mater.* **20**, 2621–2623. (doi:10.1021/cm7035579)

142. Chen X, Lou Y, Samia AC, Burda C. 2003 Coherency strain effects on the optical response of core/shell heteronanostructures. *Nano Lett.* **43**, 799–803. (doi:10.1021/nl034243b)

143. Kim S, Fisher B, Eisler HJ, Bawendi M. 2003 Type-II quantum dots: CdTe/CdSe(core/shell) and CdSe/ZnTe(core/shell) heterostructures. *J. Am. Chem. Soc.* **125**, 11 466–11 467. (doi:10.1021/ja0361749)

144. Mahler B, Spinicelli P, Buil S, Quelin X, Hermier JP, Dubertret B. 2008 Towards non-blinking colloidal quantum dots. *Nat. Mater.* **7**, 659–664. (doi:10.1038/nmat2222)

145. Wang X *et al.* 2009 Non-blinking semiconductor nanocrystals. *Nature* **459**, 686–689. (doi:10.1038/nature08072)

146. Medintz IL, Uyeda HT, Goldman ER, Mattoussi H. 2005 Quantum dot bioconjugates for imaging, labelling and sensing. *Nat. Mater.* **4**, 435–446. (doi:10.1021/ja054630i)

147. Basiruddin SK, Saha A, Pradhan N, Jana NR. 2010 Advances in coating chemistry in deriving soluble functional nanoparticle. *J. Phys. Chem. C* **114**, 11 009–11 017. (doi:10.1021/jp100844d)

148. Breus VV, Heyes CD, Nienhaus GU. 2007 Quenching of CdSe/ZnS core/shell quantum dot luminescence by water-soluble thiolated ligands. *J. Phys. Chem. C* **111**, 18 589–18 594. (doi:10.1021/jp075848p)

149. Yong K-T, Ding H, Roy I, Law W-C, Bergey EJ, Maitra A, Prasad PN. 2009 Imaging pancreatic cancer using bioconjugated InP quantum dots. *ACS Nano* **3**, 502–510. (doi:10.1021/nn8008933)

150. Tamang S, Beaune G, Texier I, Reiss P. 2011 Aqueous phase transfer of InP/ZnS nanocrystals conserving fluorescence and high colloidal stability. *ACS Nano* **5**, 9392–9402. (doi:10.1021/nn203598c)

151. Tong S, Hou S, Zheng Z, Zhou J, Bao G. 2010 Coating optimization of superparamagnetic iron oxide nanoparticles for high T2 relaxivity. *Nano Lett.* **10**, 4607–4613. (doi:10.1021/nl102623x)

152. Soo Choi H, Liu W, Misra P, Tanaka E, Zimmer JP, Itty Ipe B, Bawendi MG, Frangioni JV. 2007 Renal clearance of quantum dots. *Nat. Biotech.* **25**, 1165–1170. (doi:10.1038/nbt1340)

153. Wang M, Thanou M. 2010 Targeting nanoparticles to cancer. *Pharmacol. Res.* **62**, 90–99. (doi:10.1016/j.phrs.2010.03.005)

154. Hak S, Hegelsen E, Hektoen HH, Huuse EM, Jarzyna PA, Mulder WJM, Haraldseth O, de Lange Davies C. 2012 The effect of nanoparticle polyethylene glycol surface density on ligand-directed tumor targeting studied *in vivo* by dual modality imaging. *ACS Nano* **6**, 5648–5658. (doi:10.1021/nn301630n)

155. Lee H, Lee E, Kim DK, Jang NK, Jeong YY, Jon S. 2006 Antibiofouling polymer-coated superparamagnetic iron oxide nanoparticles as potential magnetic resonance contrast agents for *in vivo* cancer imaging. *J. Am. Chem. Soc.* **128**, 7383–7389. (doi:10.1021/ja061529k)

156. Wilhelm C, Gazeau F. 2008 Universal cell labelling with anionic magnetic nanoparticles. *Biomater.* **29**, 3161–3174. (doi:10.1016/j.biomaterials.2008.04.016)

157. Villanueva A, Canete M, Roca AG, Calero M, Veintemillas-Verdaguer S, Serna CJ, del Puerto Morales M, Miranda R. 2009 The influence of surface functionalization on the enhanced internalization of magnetic nanoparticles in cancer cells. *Nanotechnology* **20**, 115103. (doi:10.1088/0957-4484/20/11/115103)

158. Sun C, Lee JSH, Zhang M. 2008 Magnetic nanoparticles in MR imaging and drug delivery. *Adv. Drug Del. Rev.* **60**, 1252–1265. (doi:10.1016/j.addr.2008.03.018)

159. Chou S-W, Shau Y-H, Wu P-C, Yang Y-S, Shieh D-B, Chen C-C. 2010 *In vitro* and *in vivo* studies of FePt nanoparticles for dual modal CT/MRI molecular imaging. *J. Am. Chem. Soc.* **132**, 13 270–13 278. (doi:10.1021/ja1035013)

160. Mattoussi H, Palui G, Na HB. 2012 Luminescent quantum dots as platforms for probing *in vitro* and *in vivo* biological processes. *Adv. Drug. Deliv. Rev.* **64**, 138–166. (doi:10.1016/j.addr.2011.09.011)

161. Kim S *et al.* 2004 Near-infrared fluorescent type II quantum dots for sentinel lymph node mapping. *Nat. Biotechnol.* **22**, 93–97. (doi:10.1038/nbt920)

162. Deng D, Chen Y, Cao J, Tian J, Qian Z, Achilefu S, Gu Y. 2012 High-quality CuInS₂/ZnS quantum dots for *in vitro* and *in vivo* bioimaging. *Chem. Mater.* **24**, 3029–3037. (doi:10.1021/cm3015594)

163. Li L, Daou TJ, Texier I, Chi TTK, Liem NQ, Reiss P. 2009 Highly luminescent CuInS2/ZnS core/shell nanocrystals: cadmium-free quantum dots for *in vivo* imaging. *Chem. Mater.* **21**, 2422–2429. (doi:10.1021/cm900103b)

164. Pons T, Pic E, Lequeux N, Cassette E, Bezdetnaya L, Guillemin F, Marchal F, Dubertret B. 2010 Cadmium-free CuInS₂/ZnS quantum dots for sentinel lymph node imaging with reduced toxicity. *ACS Nano* **4**, 2531–2538. (doi:10.1021/nn901421v)

165. Park J, Dvoracek C, Lee KH, Galloway JF, Bhang H-EC, Pomper MG, Searson PC. 2011 CuInSe/ZnS core/shell NIR quantum dots for biomedical imaging. *Small* **7**, 3148–3152. (doi:10.1002/smll.201101558)

166. Gao J, Chen K, Luong R, Bouley DM, Mao H, Qiao T, Gambhir SS, Cheng Z. 2012 A novel clinically translatable fluorescent nanoparticle for targeted molecular imaging of tumors in living subjects. *Nano Lett.* **12**, 281–286. (doi:10.1021/nl203526f)

167. Jarzyna PA, Gianella A, Skajaa T, Knudsen G, Deddens LH, Cormode DP, Fayad ZA, Mulder WJM. 2010 Multifunctional imaging nanoprobes. *WIREs Nanomed. Nanobiotech.* **2**, 138–150. (doi:10.1002/wnan.72)

168. Hao R, Wing R, Xu Z, Hou Y, Gao S, Sun S. 2010 Synthesis, functionalization, and biomedical applications of multifunctional magnetic nanoparticles. *Adv. Mater.* **22**, 2729–2742. (doi:10.1002/adma.201000260)

169. Corr SA, Rakovich YP, Gun'ko YK. 2008 Multifunctional magnetic-fluorescent nanocomposites for biomedical applications. *Nanoscale Res. Lett.* **3**, 87–104. (doi:10.1007/s11671-008-9122-8)

170. Ho D, Sun X, Sun S. 2011 Monodisperse magnetic nanoparticles for theranostic applications. *Acc. Chem. Res.* **44**, 875–882. (doi:10.1021/ar200090c)

171. Zanella M, Falqui A, Kudera S, Manna L, Casula MF, Parak WJ. 2008 Growth of colloidal nanoparticles of group II–VI and IV–VI semiconductors on top of magnetic iron-platinum nanocrystals. *J. Mater. Chem.* **18**, 4311–4317. (doi:10.1039/b804154g)

172. Trinh TT, Mott D, Thanh NTK, Maenosono S. 2011 One-pot synthesis and characterization of well defined core-shell structure FePt@CdSe nanoparticles. *RSC Adv.* **1**, 100–108. (doi:10.1039/c1ra00012h)

173. Gu H, Zheng R, Zhang X, Xu B. 2004 Facile one-pot synthesis of bifunctional heterodimers of nanoparticles: a conjugate of quantum dot and magnetic nanoparticles. *J. Am. Chem. Soc.* **126**, 5664–5665. (doi:10.1021/ja0496423)

174. Maynadié J, Salant A, Falqui A, Respaud M, Shaviv E, Banin U, Soulantica K, Chaudret B. 2008 Cobalt growth on the tips of CdSe nanorods. *Angew. Chem. Int. Ed.* **48**, 1814–1817. (doi:10.1002/anie.200804798)

175. Gao J, Zhang W, Huang P, Zhang B, Zhang X, Xu B. 2008 Intracellular spatial control of fluorescent magnetic nanoparticles. *J. Am. Chem. Soc.* **130**, 3710–3711. (doi:10.1021/ja7103125)

176. Shen J-M, Guan X-M, Liu X-Y, Lan J-F, Cheng T, Zhang H-X. 2012 Luminescent/magnetic hybrid nanoparticles with folate-conjugated peptide composited for tumor-targeted drug delivery. *Bioconjug. Chem.* **23**, 1010–1021. (doi:10.1021/bc300008k)

177. Bigall NC, Parak WJ, Dorfs D. 2012 Fluorescent, magnetic and plasmonic-hybrid multifunctional colloidal nano objects. *Nano Today* **7**, 282–296. (doi:10.1016/j.nantod.2012.06.007)

178. Deka S *et al.* 2009 Fluorescent asymmetrically cobalt-tipped CdSe@CdS core@shell nanorod heterostructures exhibiting room-temperature ferromagnetic behavior. *J. Am. Chem. Soc.* **131**, 12 817–12 828. (doi:10.1021/ja904493c)